Diffuse radio emission from galaxy clusters in the LOFAR Two-metre Sky Survey Deep Fields

E. Osinga, R. van Weeren, J. Boxelaar, G. Brunetti, A. Botteon, M. Brüggen, T. Shimwell, A. Bonafede, P. Best, M. Bonato, et al.

A&A 648, A11 (2021)
https://doi.org/10.1051/0004-6361/202039076

Astronomy & Astrophysics

The LOFAR Two Meter Sky Survey

Special issue

Diffuse radio emission from galaxy clusters in the LOFAR Two-metre Sky Survey Deep Fields

E. Osinga[1], R. J. van Weeren[1], J. M. Boxelaar[1], G. Brunetti[2], A. Botteon[1], M. Brüggen[3], T. W. Shimwell[4,1], A. Bonafede[5,2], P. N. Best[6], M. Bonato[2,7,8], R. Cassano[2], F. Gastaldello[9], G. di Gennaro[1], M. J. Hardcastle[10], S. Mandal[1], M. Rossetti[9], H. J. A. Röttgering[1], J. Sabater[6], and C. Tasse[11,12]

[1] Leiden Observatory, Leiden University, PO Box 9513, 2300 RA Leiden, The Netherlands
e-mail: osinga@strw.leidenuniv.nl
[2] Istituto Nazionale di Astrofisica, Istituto di Radioastronomia Via P Gobetti 101, 40129 Bologna, Italy
[3] Hamburg Observatory, University of Hamburg, Gojenbergsweg 112, 21029 Hamburg, Germany
[4] ASTRON, the Netherlands Institute for Radio Astronomy, Postbus 2, 7990 AA Dwingeloo, The Netherlands
[5] DIFA – Universitá di Bologna, Via Gobetti 93/2, 40129 Bologna, Italy
[6] SUPA, Institute for Astronomy, Royal Observatory, Blackford Hill, Edinburgh, EH9 3HJ, UK
[7] Italian ALMA Regional Centre, Via Gobetti 101, 40129 Bologna, Italy
[8] INAF – Osservatorio Astronomico di Padova, Vicolo dell'Osservatorio 5, 35122 Padova, Italy
[9] INAF – IASF Milano, Via A. Corti 12, 20133 Milano, Italy
[10] Centre for Astrophysics Research, University of Hertfordshire, College Lane, Hatfield AL10 9AB, UK
[11] GEPI, Observatoire de Paris, CNRS, Université Paris Diderot, 5 place Jules Janssen, 92190 Meudon, France
[12] Department of Physics & Electronics, Rhodes University, PO Box 94, Grahamstown 6140, South Africa

Received 31 July 2020 / Accepted 26 January 2021

ABSTRACT

Low-frequency radio observations are revealing an increasing number of diffuse synchrotron sources from galaxy clusters, primarily in the form of radio halos or radio relics. The existence of this diffuse synchrotron emission indicates the presence of relativistic particles and magnetic fields. It is still an open question as to exactly what mechanisms are responsible for the population of relativistic electrons driving this synchrotron emission. The LOFAR Two-metre Sky Survey Deep Fields offer a unique view of this problem. Reaching noise levels below 30 μJy beam^{-1}, these are the deepest images made at the low frequency of 144 MHz. This paper presents a search for diffuse emission in galaxy clusters in the first data release of the LOFAR Deep Fields. We detect a new high-redshift radio halo with a flux density of 8.9 ± 1.0 mJy and corresponding luminosity of $P_{144\mathrm{MHz}} = (3.6 \pm 0.6) \times 10^{25}$ W Hz^{-1} in an X-ray detected cluster at $z = 0.77$ with a mass estimate of $M_{500} = 3.3^{+1.1}_{-1.7} \times 10^{14} M_{\odot}$. Deep upper limits are placed on clusters with non-detections. We compare the results to the correlation between halo luminosity and cluster mass derived for radio halos found in the literature. This study is one of a few to find diffuse emission in low mass ($M_{500} < 5 \times 10^{14} M_{\odot}$) systems and shows that deep low-frequency observations of galaxy clusters are fundamental for opening up a new part of parameter space in the study of non-thermal phenomena in galaxy clusters.

Key words. galaxies: clusters: general – galaxies: clusters: intracluster medium – radiation mechanisms: non-thermal – radio continuum: general

1. Introduction

Galaxy clusters are the largest virialised conglomerations of baryons and dark matter in the Universe as well as the densest parts of the large-scale matter structure of the Universe. An increasing number of galaxy clusters are revealing diffuse synchrotron radio emission, which indicates the presence of magnetic fields and a pool of relativistic electrons in the intracluster medium (ICM; van Weeren et al. 2019). The properties and origin of the pool of relativistic electrons are still not fully clear (Brunetti & Jones 2014), and neither are the exact properties of the magnetic fields of galaxy clusters (Donnert et al. 2018).

The diffuse radio emission in merging galaxy clusters has been broadly classified into two main classes: radio halos and radio relics (Feretti et al. 2012; van Weeren et al. 2019). Radio halos are diffuse radio structures that roughly follow the thermal ICM distribution as observed by X-ray observations. Radio relics, also called radio shocks, are elongated and polarised structures found in the outskirts of galaxy clusters that are tracing merger-induced shock waves (Brunetti & Jones 2014; Brüggen et al. 2012).

The currently favoured model for radio halos is the turbulent re-acceleration model, which poses that merger-induced turbulence (re-)accelerates cosmic-ray electrons which produce the radio halo (e.g. Brunetti & Lazarian 2007; Paul et al. 2011; Miniati 2015). The turbulent re-acceleration model is supported by observations that show that radio halos are generally found in merging systems (e.g. Cassano 2010; Cassano et al. 2013; Wen & Han 2013; Kale et al. 2015; Cuciti et al. 2015; Eckert et al. 2017). A possible contribution may come from the hadronic model, which states that relativistic electrons are products of hadronic collisions between relativistic protons and thermal ions (e.g. Blasi & Colafrancesco 1999; Dolag & Enßlin 2000). However, upper limits to gamma-ray emission expected from the decay products, in particular upper limits on the Coma cluster

(e.g. Jeltema & Profumo 2011; Zandanel & Ando 2014; Brunetti et al. 2012, 2017), and the very steep spectra observed in a fraction of radio halos (e.g. Brunetti et al. 2008; Wilber et al. 2017) rule out a dominant contribution from this channel, although a scenario where secondaries are re-accelerated by turbulence is not excluded (e.g. Brunetti & Lazarian 2011; Pinzke et al. 2017; Brunetti et al. 2017).

Radio halos are more commonly found in higher-mass clusters, owing to the known scaling relation between the radio power and host cluster X-ray luminosity or mass (Liang et al. 2000; Cassano et al. 2013; Bîrzan et al. 2019). This scaling relation was found to exhibit a bi-modal behaviour, with merging systems lying on the correlation and with more relaxed systems generally being less luminous or undetected in the radio band at a level significantly below the correlation (e.g. Cassano et al. 2013; Cuciti et al. 2015). This behaviour corroborates the idea that the kinetic energy dissipated during merger events powers radio halos.

Some exceptions to the scaling relation and merger connection have been found. There are a few cases of over-luminous radio halos (i.e. halos found in low X-ray luminosity clusters) (e.g. Giovannini et al. 2009, 2011), although with only a few detections, the classification of these sources remains uncertain. Radio halos have also been found to be present in (semi-) relaxed clusters (Bonafede et al. 2014; Sommer et al. 2017; Savini et al. 2019), suggesting that minor mergers in massive clusters might also have the potential to dissipate enough energy to power cluster-scale emission, although again, these are only a few examples.

Most radio halos observed at gigahertz frequencies have spectral indices slightly lower than $\alpha = -1$ (where $S_\nu \propto \nu^\alpha$) (Giovannini et al. 2009; Feretti et al. 2012). In a number of cases, ultra-steep ($\alpha < -1.6$) spectrum radio halos (USSRH) have been observed (e.g. Dallacasa et al. 2009; Macario et al. 2013; Wilber et al. 2017). The turbulent re-acceleration model predicts that less energetic mergers, often associated with lower mass systems, could generate halos with lower synchrotron break frequencies (<1GHz) (Cassano 2010). Observing radio halos close to the break frequency leads to finding steeper spectrum halos. Because USSRHs are expected to be discovered at low frequencies, and to be associated mainly to low mass clusters, the correlation between the radio halo luminosity at 120 MHz and the X-ray luminosity of the cluster is predicted to be steeper and more scattered than at higher radio frequencies (Cassano 2010).

There are still many open questions relating to the origin and formation of radio halos. Due to the higher occurrence rate and radio luminosity of halos with increasing cluster mass (Cassano et al. 2013; Cuciti et al. 2015), most of the understanding has been built on studies of relatively massive ($>5 \times 10^{14} M_\odot$) galaxy clusters. However, it is important to study radio halos in low mass systems to understand their origin. Only a few radio halos have been detected below cluster masses of $5 \times 10^{14} M_\odot$, with the lowest mass cluster being A3562 (Venturi et al. 2003) at $2.44^{+0.21}_{-0.24} \times 10^{14} M_\odot$ (see Bîrzan et al. 2019, for a recent compilation of halos from the literature).

The fact that the turbulent re-acceleration model predicts that an increasing fraction of halos in lower mass clusters should have a steep spectrum implies that lower mass systems should be more easily detected at lower frequencies (e.g. Cassano 2010; Brunetti & Jones 2014). Furthermore, less massive clusters have a smaller turbulent energy budget, which implies that the effect of turbulent re-acceleration may become less dominant at lower cluster masses. Consequently, a possible transition from turbulent halos to halos powered by hadronic interactions is predicted (e.g. Cassano et al. 2012; Brunetti & Jones 2014). The transition depends on the amount of cosmic ray protons available in galaxy clusters, which is still not understood.

The LOFAR Deep Fields (Tasse et al. 2021; Sabater et al. 2021; Kondapally et al. 2021; Duncan et al. 2021) are a set of deep LOFAR observations on three fields which have high-quality multi-wavelength ancillary data available. These fields provide a unique opportunity to study radio halos in the low-mass and low luminosity regime due to the low-frequency and large depth of the observations. This relatively unexplored regime can elucidate mechanisms of halo formation in low mass clusters that exhibit lower levels of turbulent motions. In this paper, we present a search for diffuse emission associated with galaxy clusters in the LOFAR Deep Fields. Throughout, we assume a flat ΛCDM cosmology with $H_0 = 70\,\mathrm{km s^{-1}\,Mpc^{-1}}$, $\Omega_m = 0.3$ and $\Omega_\Lambda = 0.7$. We define the spectral nature of the radio emission as $S_\nu \propto \nu^\alpha$ where S_ν is the measured flux density at the frequency ν and α is the spectral index.

2. Data

The LOFAR surveys key science project aims to survey the Northern sky at 120–168 MHz at several depth tiers with the LOFAR High Band Antenna. The wide survey aims to reach a sensitivity of 100 μJy beam^{-1}over the entire northern sky (Shimwell et al. 2017, 2019), while the Deep Fields are a set of deeper images of a few selected fields. This paper makes use of the first data release of the LOFAR Two Metre Sky Survey (LoTSS) Deep Fields (Tasse et al. 2021; Sabater et al. 2021; Kondapally et al. 2021; Duncan et al. 2021), which currently consists of three fields with a wealth of multi-wavelength data available: the European Large-Area ISO Survey-North 1 (ELAIS-N1; Oliver et al. 2000), Boötes (Jannuzi & Dey 1999) and the Lockman Hole (Lockman et al. 1986), which cover a combined area of >50 deg^2. The final aim of the LoTSS Deep Fields is to reach noise levels of 10−15 μJy beam^{-1} (Tasse et al. 2021) near the pointing centre.

In the first data release, the Lockman Hole and Boötes field were observed for 80 and 112 h, reaching noise levels in the centre of the fields of ∼22 and 32 μJy beam^{-1} respectively. The observations and data reduction process of these two fields are described in detail by Tasse et al. (2021). The ELAIS-N1 field was observed for 170 h, reaching noise levels of ∼20 μJy beam^{-1}. This field required a custom data reduction strategy due to a different observing setup and bandwidth coverage, which is detailed by Sabater et al. (2021).

3. Methods

We identified all clusters within 2.5 degrees of the pointing centre in the ELAIS-N1 and Lockman Hole fields that were present in the second *Planck* catalogue of Sunyaev-Zel'dovich detected sources (PSZ2; Planck Collaboration XXVII 2016), the Meta-Catalogue of X-ray detected Clusters of galaxies (MCXC; Piffaretti et al. 2011) or the Combined *Planck*-RASS catalogue of X-ray-SZ clusters (ComPRASS; Tarrío et al. 2019). Seven clusters in the aforementioned catalogues are present in the deep fields, of which the details are given in Table 1. We also checked the optically (SDSS data) selected cluster catalogue WHL (Wen et al. 2012) for clusters showing signs of diffuse emission and visually identified three more clusters that show hints of diffuse emission, although these are more likely to be AGN-related extended emission. Finally, we also add the SpARCS1049+56

Table 1. Sample of sources extracted from the LOFAR Deep Fields.

Source name	Field	Redshift	M_{500} ($10^{14} M_\odot$)	R_{500} (Mpc)	Radio classification
MCXC J1033.8+5703	Lockman	0.0463	0.128	0.35	No detection
MCXC J1036.1+5713	Lockman	0.7699	3.25	0.78	Halo
MCXC J1053.3+5720	Lockman	0.34	0.487	0.49	No detection
PSZ2 G147.88+53.24	Lockman	0.60	6.47 ± 0.60	1.06	Halo
PSZ2 G149.22+54.18	Lockman	0.1369	$5.87^{+0.23}_{-0.22}$	1.22	Halo
SpARCS1049+56	Lockman	1.71 [(1)]	2.52 ± 0.86 [(2)]	0.51	AGN
SDSSC4-3094	Lockman	0.04632 [(3)]			AGN
PSZRX G084.01+46.28	ELAIS-N1	0.0675	$1.37^{+0.33}_{-0.36}$	0.77	No detection
PSZ2 G084.69+42.28	ELAIS-N1	0.13	$2.70^{+0.27}_{-0.26}$	0.94	Uncertain
WHL J160439.5+543139	ELAIS-N1	0.2655	2.95 ± 0.50	0.93	Detection uncertain
WHL J161135.9+541635	ELAIS-N1	0.3407	3.40 ± 0.58	0.94	No detection
WHL J161420.1+544254	ELAIS-N1	0.3273	2.85 ± 0.48	0.89	Detection uncertain

Notes. The mass, redshift and R_{500} are obtained from the PSZ2 catalogue (Planck Collaboration XXVII 2016) or from the MCXC catalogue (Piffaretti et al. 2011) if the source was not present in the former catalogue, unless otherwise noted. For the WHL clusters M_{500} was estimated from the richness, as detailed in Sect. 5.7. Mass uncertainties are not available for MCXC clusters.

References. [(1)]Webb et al. (2015). [(2)]Derived from M_{200} given in Finner et al. (2020), see Sect. 5.5. [(3)]Miller et al. (2005).

cluster to our sample, which was identified by Webb et al. (2015) to be a very high redshift ($z = 1.71$) cluster in the Lockman Hole field. As a fortuitous bonus, the cluster SDSSC4-3094 identified in the Sloan Digital Sky Survey (Miller et al. 2005) at $z = 0.04632 \pm 0.00083$ lies in the same region of the sky as SpARCS1049+56 and is therefore added to the sample. Details on the total of 12 clusters are given in Table 1, seven and five of which are in Lockman and ELAIS-N1 respectively. The Boötes deep field observations do not overlap with any clusters from the PSZ2, MCXC or ComPRASS catalogues. No clear diffuse emission from cluster objects was picked up from visual identification of the field, including the 12 spectroscopically confirmed clusters at $z > 1$ found by Eisenhardt et al. (2008).

3.1. Target extraction and imaging

Once clusters are identified, we followed an 'extract and subtract' procedure to optimise the sensitivity of the deep images to diffuse emission in the direction of the cluster by allowing for easy re-imaging. First, we made small ($\sim 0.3^\circ \times 0.3^\circ$) boxes around the identified targets. The *uv*-data corresponding to this box were extracted from the full dataset with the following method. A direction-dependent calibrated model, from the pipeline described in Tasse et al. (2021) and Sabater et al. (2021), of all components outside the boxed region was subtracted from the model data. This leaves visibilities that contain only sources in the boxed region. We then phase-shifted to the centre of the extracted region, averaged the data in time and frequency to reduce the size and performed 7 rounds of direction dependent self calibration with the DDF pipeline[1] (Tasse 2014; Smirnov & Tasse 2015; Tasse et al. 2018) to improve the quality of the extracted image compared to that in the original deep field maps. In the original deep field maps, the facets used for direction dependent calibration are larger as the distance to the pointing centre increases, causing more calibration errors related to the assumed constant beam model and ionosphere over a single facet. This extraction procedure mitigates these errors by manually defining a smaller sub-region than the original facet around the target of interest. The primary beam correction on these extracted and self-calibrated visibilities was done by multiplication with a constant factor of the primary beam response at the centre of the extracted region, which is a good assumption, since the extraction region is much smaller than the size of the LOFAR primary beam (full width at half maximum $\sim 2.5^\circ$). The details of the extraction process are described in van Weeren et al. (2020) and the method has been used with various other LOFAR observations (e.g. Hardcastle et al. 2019; Mandal et al. 2020; Botteon et al. 2020a,b).

To properly disentangle the extended diffuse emission from compact sources, compact sources were subtracted. This was done as follows: first, an image of only the compact sources was made by ignoring short baselines that are sensitive to extended emission. The inner *uv*-cut was initially calculated such that it corresponds to emission of a certain largest linear physical size at the cluster redshift, based on the mass of the cluster. As an example, for the low mass system MCXCJ1036.1+5713 we found that the *uv*-cut of 2547λ (i.e. 600 kpc at $z = 0.76991$) was too small to properly exclude all diffuse emission. A *uv*-cut of 3820λ (i.e. 400 kpc) shows better separation of diffuse emission and compact sources, as shown in Fig. 1. As higher mass clusters often have larger radio halos, it makes sense to have lower *uv*-cuts (in kpc) with lower cluster mass.

The clean component model of the compact image was subtracted from the visibilities of the extracted dataset, leaving only the visibilities corresponding to the diffuse extended emission. This emission was imaged with a Gaussian taper corresponding to 50 kpc at the cluster redshift, using multi-scale clean, with `WSClean` (version 2.7.3) (Offringa et al. 2014; Offringa & Smirnov 2017) to properly deconvolve the diffuse emission. The complete compact source subtraction process is illustrated in Fig. 1 for the cluster MCXCJ1036.1+5713 as an example.

3.2. Measuring radio halo properties

To measure the properties of the diffuse emission, we fitted the radio halos with an exponential profile. This has a few advantages over manually defining the halo region. Commonly, the radio halo flux density is measured by integrating the surface brightness over an area bounded by isophotes (e.g. 3σ contours). However, this causes the resulting flux density to be dependent on the sensitivity of the observations. It is more rigorous to fit the halos with a profile and analytically integrate that profile up to

[1] https://github.com/mhardcastle/ddf-pipeline

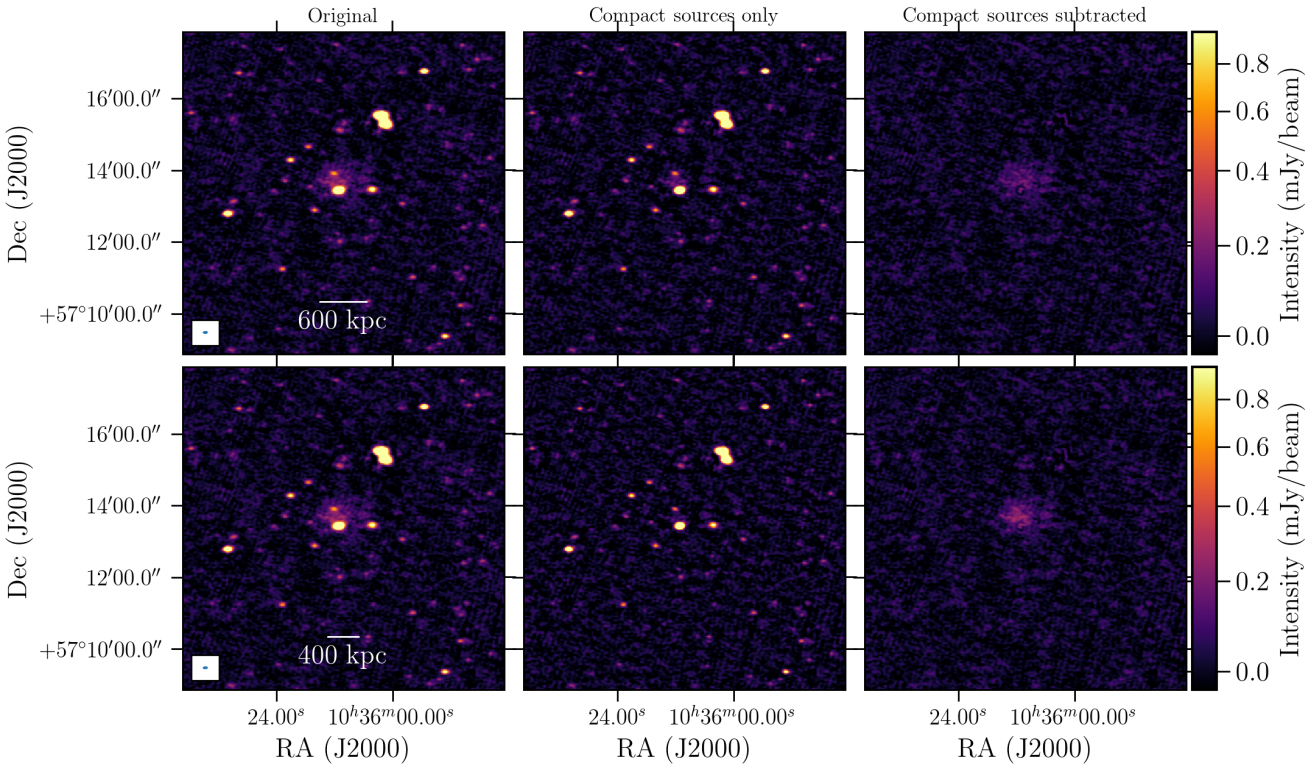

Fig. 1. Compact source subtraction process for the cluster MCXCJ1036.1+5713. *Left column*: original image, *middle column*: image containing only the compact emission, and *right column*: final compact source subtracted image. All images are made with the same parameters, except the *uv*-cut for the central image. The top compact source only image was made with a *uv*-cut of 2547λ (i.e. 600 kpc at the cluster redshift) while the bottom image was made with a *uv*-cut of 3820λ (i.e. 400 kpc). The restoring beam size is $9'' \times 5''$.

a certain radius. It has been shown that exponential profiles can provide characteristic scales relatively independent of the sensitivity of the radio observations (Murgia et al. 2009). In this work we consider the simplest, spherically symmetric, exponential profile for most of the halos, which has been found to be representative of radio halos (Murgia et al. 2009), although in some cases observations of radio halos have shown strong deviations from spherical symmetry (e.g. van Weeren et al. 2016; Wang et al. 2018). The surface brightness model is given by

$$I(\boldsymbol{r}) = I_0 e^{-\boldsymbol{r}/r_e}, \tag{1}$$

where I_0 and r_e are the central surface brightness and the e-folding radius, respectively. To compare the e-folding radii of the halos to the radii of the halos that are normally quoted in the literature (r_H), we assume $r_H/r_e = 2.6$, as was found by Bonafede et al. (2017) for 8 clusters with measured r_H within 3σ isophotes and fitted r_e.

The presented fitting of Eq. (1) and halo radio flux density estimations were done with a newly developed algorithm[2]. The algorithm is described in detail by Boxelaar et al. (2021), and we briefly explain it here. The fitting algorithm is based on fitting methods first presented by Murgia et al. (2009). The difference here is that profiles are fitted to a two-dimensional image directly rather than to a radially averaged one-dimensional data array. This allows fitting of a non-circular model as well, although for simplicity we assume a circular model in this work. Theoretically, one could fit both a circular and a non-circular model and compare a goodness of fit statistic (e.g. reduced χ^2) of both models to determine which model is a better fit. However, the determination of the morphology of the diffuse emission is beyond the goal of this paper and requires high signal-to-noise data to determine statistically significant differences in the goodness of fit statistic.

The total flux density S of the fitted radio emission is obtained by integrating Eq. (1). The analytical expression for the total flux density is $S = 2\pi I_0 r_e^2 \left(1 - e^{-d}(d+1)\right)$, where d denotes the radius (in e-folding radii) up to which is being integrated. Here we choose to integrate up to $2.6r_e$, following Bonafede et al. (2017). For comparison, integrating up to $2.6r_e$ results in a total flux density that is 73% of the flux density found when integrating the model to infinity.

The best-fit estimates for the peak surface brightness and e-folding radius are found through Bayesian inference and maximum likelihood estimation. To sample the likelihood function, we use a Monte Carlo Markov chain, implemented within the `emcee` module (Foreman-Mackey et al. 2013). This method allows us to find the full posterior distribution for the model parameters. Given observed data $V(\boldsymbol{r}_i)$ (which represents the radio surface brightness at position $\boldsymbol{r}_i$) and fit parameter vector $\boldsymbol{\theta} = (I_0, r_e)$, we assume that all the compact source subtracted images can be expressed as $V(\boldsymbol{r}_i) = I(\boldsymbol{r}_i) + \epsilon_i$ where $I(\boldsymbol{r})$ is defined in Eq. (1) and the underlying noise ϵ_i is independent and identically distributed as $\mathcal{N}(0, \sigma^2_{\rm rms})$. Independence of individual pixels is assured through re-gridding the images such that the pixel area approximately equals the beam area, while preserving the total flux. The probability density function $f(\boldsymbol{r}_i; \boldsymbol{\theta})$ for an observation then reads

$$f(\boldsymbol{r}_i; \theta) = \frac{1}{\sqrt{2\pi}\sigma_{\rm rms}} \exp\left(-\frac{(V(\boldsymbol{r}_i) - I(\boldsymbol{r}_i; \theta))^2}{2\sigma^2_{\rm rms}}\right). \tag{2}$$

[2] https://github.com/JortBox/Halo-FDCA

This results in a log likelihood function which is given by

$$\ln \mathcal{L}(\theta) = -n \ln \sqrt{2\pi}\sigma_{\rm rms} - \frac{1}{2\sigma^2_{\rm rms}} \sum_{i=1}^{n} (V(\boldsymbol{r}_i) - I(\boldsymbol{r}_i;\theta))^2, \quad (3)$$

where the sum is taken over the n re-gridded pixels. Maximising the log-likelihood function for θ allows us to find the best-fit model parameter vector $\hat{\theta}$.

The uncertainty of the total flux density of the halos f_H is calculated by adding the uncertainty due to map noise (i.e. the uncertainty on best-fit parameters $\sigma_{\rm fit}$), the absolute flux density scale $\delta_{\rm cal}$ and compact source subtraction $\sigma_{\rm sub}$ in quadrature (cf. Cassano et al. 2013).

$$\sigma_{f_H} = \sqrt{(\delta_{\rm cal} f_H)^2 + \sigma^2_{\rm fit} + \sigma^2_{\rm sub}}. \quad (4)$$

The uncertainty on the best-fit parameters $\sigma_{\rm fit}$ is given by the 16th and 84th percentile of the converged MCMC chain (i.e. 1σ) and we assume a 10% error on the absolute flux scale of the LOFAR images $\delta_{\rm cal}$ (Sabater et al. 2021) and a 1% error on the compact source subtraction process $\sigma_{\rm sub}$. The latter error is calculated as 1% of the flux contained in the compact sources only image within $2.6r_e$ of the centre of the fitted halo. This 1% error is consistent with measuring the residual flux in the compact source subtracted images at the location of bright compact sources.

For determining the upper limits in the case of non-detections, we used a similar method to that of Bonafede et al. (2017), which injects mock halos into the visibility data (see also Brunetti et al. 2007; Venturi et al. 2008). We injected mock halos following the exponential profile in Eq. (1). Following Bonafede et al. (2017), we added power spectrum fluctuations of the form $P(\Lambda) \propto \Lambda^n$, where Λ is the spatial scale, to account for surface brightness fluctuations observed in real radio halos. We set Λ between 10–250 kpc and $n = 11/3$ (Govoni et al. 2005, 2006; Bonafede et al. 2017).

The initial value of I_0 and r_e were chosen such that the expected radio power of the halo follows the $P_{1.4\rm GHz} - M_{500}$ correlation by Cassano et al. (2013). Specifically, we first calculated $P_{1.4\rm GHz}$ from the cluster mass, then set r_e according to the correlation between $P_{1.4\rm GHz} - r_e$ given by Murgia et al. (2009) and finally scaled I_0 such that the exponential model integrates up to the expected radio power of the halo. The resulting model was injected (i.e. Fourier transformed and added) into the visibility data at a location close to the cluster but absent of contaminating radio sources. The data were then cleaned and imaged in the same way as the original image. We define the halo as detected if the $3\sigma_{\rm rms}$ contours cover at least 3 beams. Provided the halo is detected, the I_0 was gradually lowered by steps of $\sigma_{\rm rms}$ to find a more stringent upper limit on the radio power. Conversely, if the halo is not detected, the I_0 was gradually increased until it is detected. We inject halos close to the clusters instead of on the centre of the clusters to avoid being biased low on the upper limits. Residual emission from point sources or an undetected halo near the cluster centre might otherwise contribute to flux measurement of the injected halos. Off cluster injection does assume, however, that there are no calibration artefacts due to bright sources in the cluster.

4. Verification on simulated halos

When determining the properties of diffuse radio emission, it is important to not only keep track of the statistical uncertainties, but to also consider additional sources of error. We test in this section two main effects. The first is the effect of the limited uv coverage of radio telescopes, particularly at shorter baselines, which may cause resolving out some diffuse emission. The second is the point source subtraction process, which may also erroneously subtract some diffuse emission, depending on the uv-cut used.

To test the fitting procedure, the sensitivity of the LOFAR observations to different scales of emission and the point source subtraction process, we injected mock halos with different I_0 and r_e into a single LOFAR observation (~8 h of data) of the Lockman Hole field. The full observations are not used for this test due to the computational intensity of the imaging and point-source subtraction process on the full dataset. The local rms at the region of injection is around 100 μJy beam^{-1}. We assume a redshift of $z = 0.30$ for the conversion of the e-folding radius to angular size. We then compare the injected properties with the properties derived from fitting. Six different halos have been injected into the data, which are shown in Fig. 2.

We subtracted point sources by employing a uv-cut of 200 kpc, corresponding to 3443λ. The compact source subtracted images are then fitted following the procedure outlined in Sect. 3.2. The resulting best-fit parameters and injected parameters are given in Table 2. We find that we generally recover the correct flux density within the 68% uncertainty, although we are biased slightly higher than the injected flux density. This is because some of the central brightness structure of the mock halos is subtracted out by the compact source subtraction process. This causes generally underestimated I_0 and overestimated r_e, which also causes generally slightly overestimated S_ν of about 10%, because the integrated flux density scales with r_e^2. This bias is important to keep in mind throughout the rest of the paper. The test does show that LOFAR is sensitive to the extended emission of halos following an exponential profile, since we are not resolving out a significant amount of flux. This is in line with what for example Hoang et al. (2018) and Botteon et al. (2020a) have found for the injection of larger halos into LOFAR observations. The full observations are about a factor of ~3 deeper than the single pointing used here, so we do not expect significant difference from these results for halos with a central surface brightness down as low as $I_0 \sim 4\mu$ Jy arcsec^{-2}.

5. Results

Here we report the results of the fitting procedure for each cluster. Unless otherwise stated, we have performed the fitting on the compact source subtracted images tapered to a resolution corresponding to 50 kpc at the cluster redshift. To calculate the radio luminosity, we assume a spectral index of $\alpha = -1.5 \pm 0.2$ for clusters where spectral index estimates are not available. We choose this range to cover the typical spectra of halos, including steep-spectrum halos (van Weeren et al. 2019). The azimuthally averaged surface brightness profiles and corner plots of the MCMC chain can be found in Appendix A.

5.1. PSZ2G147.88+53.24

PSZ2 G147.88+53.24 is a massive, high-redshift ($z = 0.6$; Planck Collaboration XXVII 2016) galaxy cluster. Diffuse emission was recently reported by Di Gennaro et al. (2021), where the emission is classified as a giant radio halo. Di Gennaro et al. (2021) measure a total flux density of 14.4 ± 2.3 mJy at 144 MHz by arithmetically subtracting the radio galaxies flux densities from the total flux density at low-resolution. The diffuse emission has a largest linear size of around 700 kpc. We employ a uv-cut

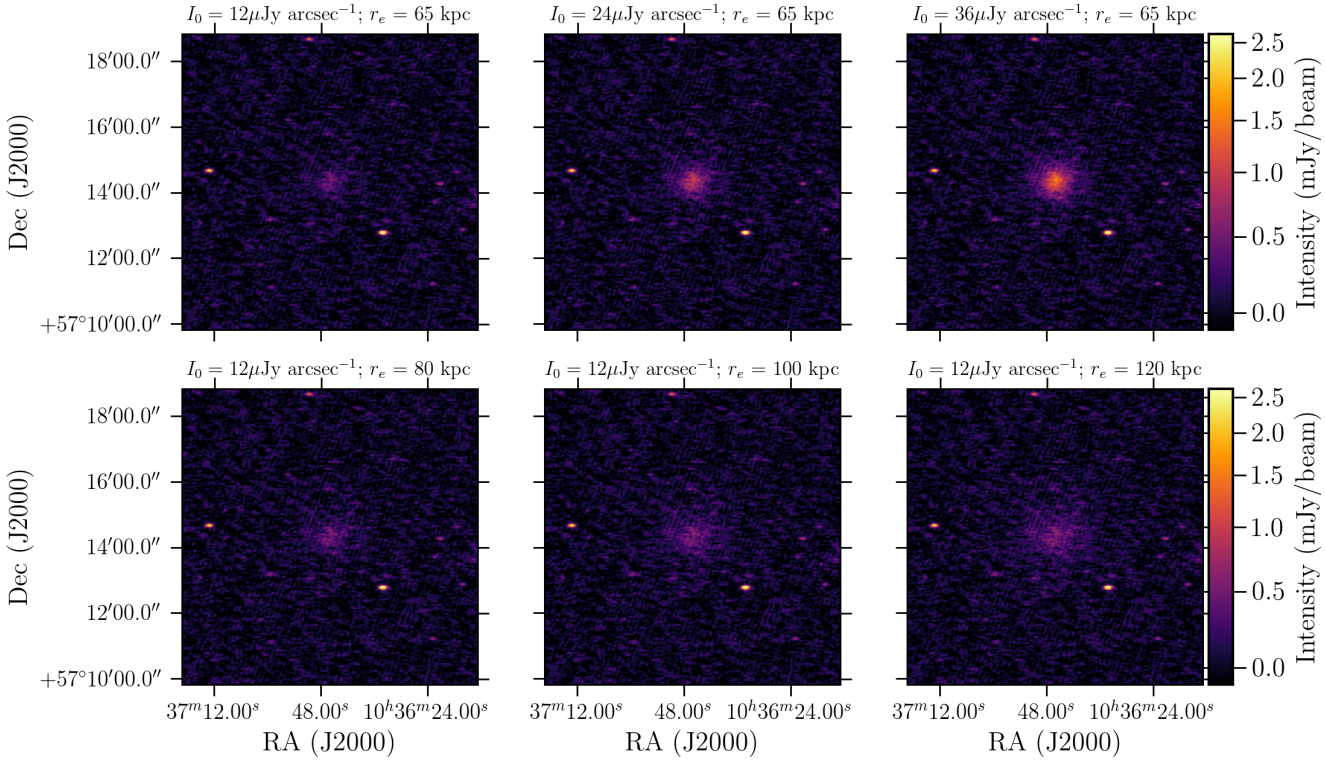

Fig. 2. Six mock halos injected into a single 8 h LOFAR observation of the Lockman Hole field. The different properties of the halos are given in the title figures.

Table 2. Results of fitting exponential profiles to mock halos of different properties.

I_0 inject [μJy arcsec^{-2}]	r_e inject [kpc]	S_ν inject [mJy]	I_0 observed [μJy arcsec^{-2}]	r_e observed [kpc]	S_ν observed [mJy]
12.0	65	20.9	$8.6^{+1.0}_{-0.9}$	82^{+8}_{-8}	23.7 ± 3.5
24.0	65	41.9	$17.3^{+0.9}_{-0.9}$	79^{+3}_{-3}	44.5 ± 5.0
36.0	65	62.8	$26.3^{+0.9}_{-0.8}$	77^{+2}_{-2}	63.8 ± 6.8
12.0	80	31.7	$10.2^{+0.8}_{-0.8}$	94^{+7}_{-6}	36.7 ± 4.7
12.0	100	49.6	$10.0^{+0.6}_{-0.7}$	118^{+7}_{-6}	57.9 ± 6.9
12.0	120	71.4	$10.2^{+0.5}_{-0.6}$	140^{+7}_{-5}	83.2 ± 9.4

Notes. The injected flux density and resulting flux density are defined as the flux fitted within $2.6r_e$. The uncertainty in the flux density here does not include an absolute flux scale uncertainty, as the injected halo flux densities would change accordingly.

corresponding to 400 kpc at the cluster redshift (3447λ) for the compact source subtraction process. We confirm the detection of Di Gennaro et al. (2021) in our deeper image, which is shown in Fig. 3 where we show the low-resolution compact source subtracted radio contours overlaid on the g, r, z optical image from the Legacy survey (Dey et al. 2019). The high-resolution radio emission is shown the right panel of Fig. 3. The source to the north-west of the central radio galaxy in Fig. 3 might be contributing to the low-resolution (compact source subtracted) radio contours, given the peculiar feature that is present in the low-resolution contours. Therefore, we decide to fit the halo with and without a mask covering the north-western source. The masked region is shown as the green region in Fig. 3.

As this cluster is at a high redshift, 50 kpc corresponds almost to the high-resolution beam size (at $z = 0.6$, 50 kpc corresponds to 7.5″). Therefore, we taper to lower resolution, using a 10″ Gaussian taper, to make the fitting procedure converge better. The full width at half maximum of the restoring beam of the low-resolution image is $21.3'' \times 18.5''$. Without any masking, the best-fit parameters are $I_0 = 4.4 \pm 0.3\,\mu$Jy arcsec^{-2}, $r_e = 194 \pm 10$ kpc. Integrating the model in Eq. (1) up to $2.6r_e$ with the best-fit parameters leads to a flux density at 144 MHz of 16.9 ± 2.0 mJy. This corresponds to a 1.4 GHz power of $P_{1.4\mathrm{GHz}} = (1.1 \pm 0.4) \times 10^{24}$ W Hz^{-1} assuming $\alpha = -1.5 \pm 0.2$. When employing the mask shown in the right panel of Fig. 3, we find best-fit parameters $I_0 = 4.5 \pm 0.3\,\mu$Jy arcsec^{-2} and $r_e = 186 \pm 11$ kpc, which correspond to a consistent integrated flux density of 16.0 ± 2.0 mJy at 144 MHz.

The resulting flux densities are a bit higher, but consistent within the error bounds with the value of 14.4 ± 2.3 mJy reported by Di Gennaro et al. (2021). This is to be expected, because our observations are deeper and Sect. 4 showed that we are likely biased a bit high on the flux density values due to the compact source subtraction process. Manually measuring the flux within 3σ contours results in slightly better agreement with a flux density of 14.7 ± 1.6 mJy.

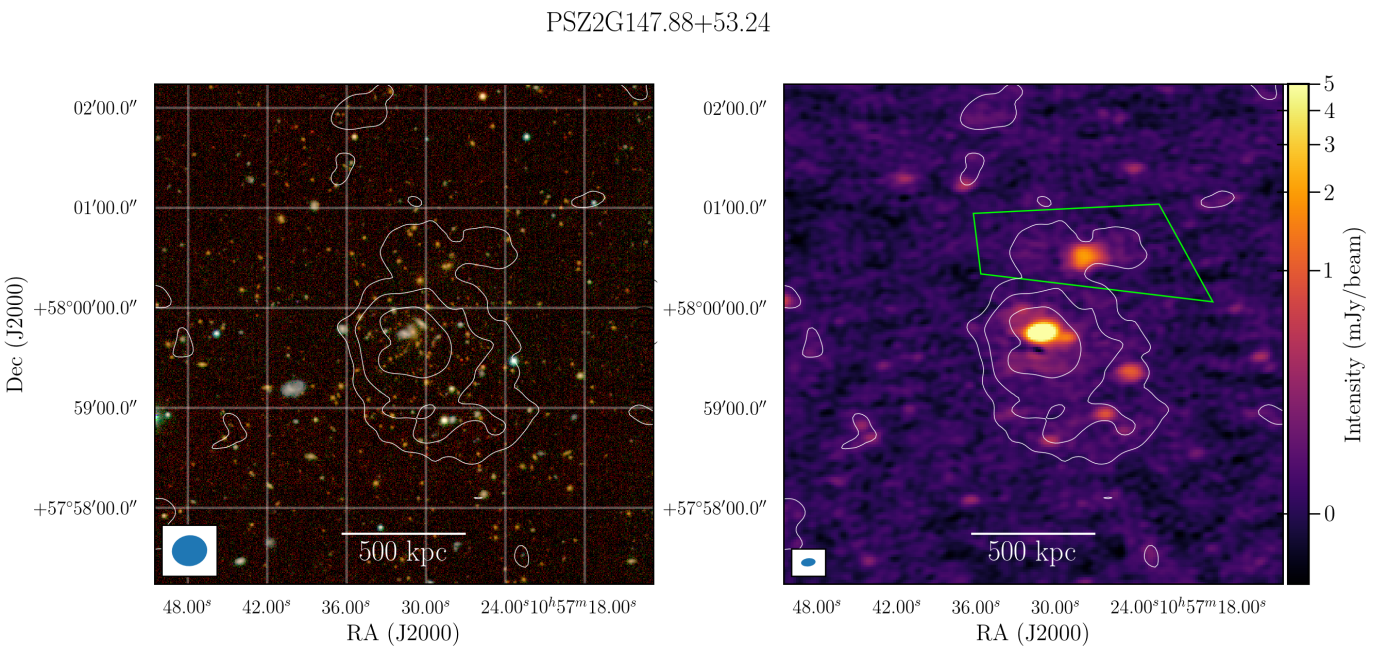

Fig. 3. Low-resolution LOFAR diffuse emission from the cluster PSZ2G147.88+53.24 overlaid on *grz* filters from the Legacy survey (Dey et al. 2019; *left*) and overlaid on the high resolution radio intensity image (*right*). The contours are plotted at $[3, 6, 12]\sigma$, where $\sigma = 83\,\mu$Jy beam^{-1}. The restoring beam sizes are $21'' \times 19''$ and $9'' \times 5''$ for the low-resolution and high-resolution radio images respectively. The green region marks the region masked from the fitting procedure.

5.2. PSZ2G149.22+54.18

PSZ2G149.22+54.18, or Abell 1132 is a quite massive cluster, with a mass of $5.87^{+0.23}_{-0.22} \times 10^{14} M_\odot$ (Planck Collaboration XXVII 2016) that is undergoing a merging event (Cuciti et al. 2015). It is located at a redshift of $z = 0.1369$ (Struble & Rood 1991). Diffuse emission was not picked up by previous VLA observations at 1.4 GHz (Giovannini & Feretti 2000), but was clearly detected by previous observations with LOFAR (Wilber et al. 2017). The central diffuse emission was classified as an ultra steep spectrum radio halo with $\alpha = -1.75 \pm 0.19$ between 144 and 325 MHz. The connection between the diffuse emission in the halo and the diffuse emission at the edge of the giant tailed radio galaxy was tentatively raised by Wilber et al. (2017), and is now clearly observed in the low-resolution contours shown in Fig. 4. We note that the halo size seems larger than previously determined, with the size inside the 3σ contours being $\sim$1.0 Mpc $\times$ 0.9 Mpc in the east-west and north-south direction, respectively.

To allow for a better comparison to the previous LOFAR observations, the compact source subtraction was done by using a *uv*-cut corresponding to 500 kpc at the cluster redshift (i.e. 1000λ in the *uv* plane). Since the giant head-tail radio galaxy blends in with the emission of the halo, we manually mask the tail from the fitting procedure. The mask is shown in the green box in Fig. 4.

The best-fit parameters are 5.7 ± 0.1 μJy arcsec^{-2} and $r_e = 235 \pm 4$ kpc. These correspond to a total flux density of the halo of 244.9 ± 29.7 mJy at 144 MHz, translating to $P_{1.4\mathrm{GHz}} = (2.5 \pm 0.3) \times 10^{23}$ W Hz^{-1}, assuming $\alpha = -1.75$, which is in agreement with the value reported by Wilber et al. (2017). The extent of the halo within the 3σ contour level is larger in our deep image than in the image of Wilber et al. (2017), which again points out that fitting the halo provides more robust flux density measurements than measuring the flux density within certain isophotes. Manually measuring the flux in the 3σ contours (without a mask) results in a flux density of 261 ± 31 mJy,

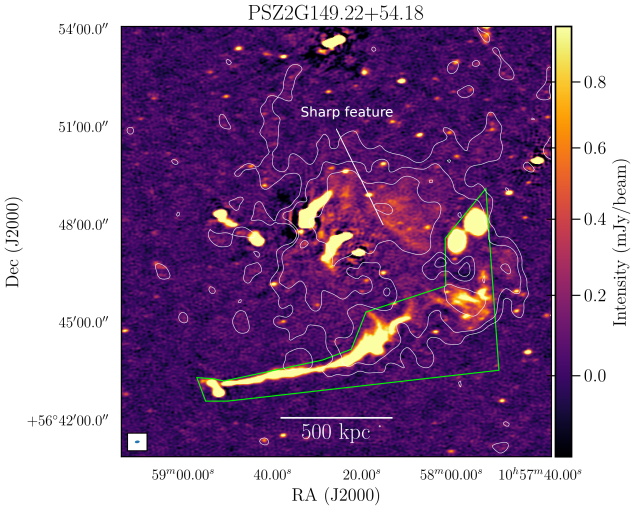

Fig. 4. High-resolution ($9'' \times 5''$) LOFAR radio intensity image of Abell 1132 with low-resolution compact source subtracted contours at $[3, 6, 12, ..]\sigma$, where $\sigma = 149\,\mu$Jy beam^{-1}. The beam size of the low-resolution contours is $28'' \times 24''$. The green box indicates the region that is masked from the fitting procedure.

which is consistent with the flux from integrating the best-fit radial profile up to $2.6r_e$. Although the halo is a bit more elongated in the east-west direction than in the north-south direction, the comparison with the manually measured flux density within 3σ contours indicates that the circular model is still a reasonable assumption.

5.3. PSZ2G084.69+42.28

PSZ2G084.69+42.28 or Abell 2201, is a relatively low mass ($2.67^{+0.27}_{-0.26} \times 10^{14} M_\odot$; Planck Collaboration XXVII 2016) galaxy cluster at a redshift of 0.13 (La Franca et al. 2002), which has

PSZ2G084.69+42.28

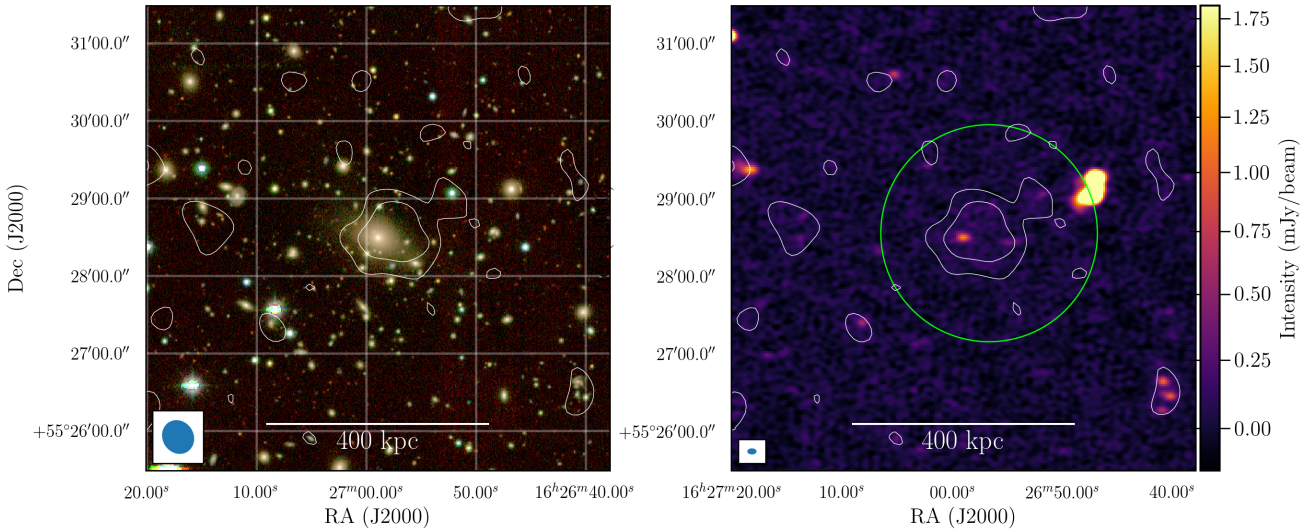

Fig. 5. Low-resolution LOFAR diffuse emission from the cluster PSZ2G084.69+42.28 overlaid on *grz* filters from the Legacy Survey (*left*) and overlaid on the high resolution radio intensity image (*right*). The contours are at $[2, 4]\sigma$, where $\sigma = 152\,\mu$Jy beam^{-1}. The high- and low-resolution beam sizes are $7'' \times 5''$ and $27'' \times 24''$ respectively. The fitting procedure was performed only within the region of the image contained by the green circle.

not been studied extensively. This cluster has the lowest mass estimate in our sample of PSZ clusters with a detection. We pick up weak diffuse emission from the cluster centre. This emission is visible in the low-resolution compact source subtracted contours overlaid on the high-resolution image in the left panel of Fig. 5. The optical image overlay is shown in the right panel, which shows that the diffuse emission surrounds the brightest cluster galaxy (BCG).

Since the diffuse emission is very small in size, we employ a *uv* cut of 2390λ, corresponding to 200 kpc at the cluster redshift. Because the emission is relatively small in size, it is possible that it is AGN-related. We enforce that the spherical profile is only fit in a region of approximately 400 kpc by masking out the outer regions, because the emission is only barely picked up above the noise. This mask is shown in the right panel of Fig. 5. The best-fit values are found to be $I_0 = 2.0^{+0.7}_{-0.6}$ μJy arcsec^{-2} and $r_e = 57^{+18}_{-13}$ kpc. Integrating the analytical model up to $2.6r_e$ results in a total flux density of 5.5 ± 1.6 mJy at 144 MHz or a radio luminosity at 144 MHz of $(2.6 \pm 0.8) \times 10^{23}$ W Hz^{-1}. Assuming a spectral index of $\alpha = -1.5 \pm 0.2$, we obtain a radio power of $P_{1.4\mathrm{GHz}} = (8.6 \pm 4.5) \times 10^{21}$ W Hz^{-1}.

Assuming $r_H/r_e = 2.6$ (Bonafede et al. 2017), the radius of the diffuse emission is about 150 kpc, which is much smaller than typical radio halos and would imply a ratio $R_H/R_{500} = 0.16$ that falls in the typical range of mini-halos (Giacintucci et al. 2017). Thus based on the size we would identify this as AGN-related emission or a mini-halo. However, according to Cassano et al. (2007) radio halos do not follow a self-similar scaling, with their size decreasing more rapidly than that of the hosting cluster with decreasing mass (see also Murgia et al. 2009). Thus, it is not unexpected that a radio halo would be smaller than halos found in high mass systems.

5.4. MCXCJ1036.1+5713

This cluster was detected by the 400 deg^2 ROSAT PSPC Galaxy Cluster Survey (Burenin et al. 2007) and lies at a redshift of $z = 0.203$ according to Piffaretti et al. (2011). However, the optical image shown in Fig. 6 does not show a clear overdensity of low-redshift galaxies, but rather shows an overdensity of small, red galaxies, which suggests that the detected cluster lies at higher redshift. Figure 7 shows the SDSS photometric redshift estimates (Ahumada et al. 2020) of galaxies within a radius of roughly 1.5′ from the central radio source, and indeed an overdensity is apparent at $z = 0.6 - 0.7$ rather than at $z = 0.2 - 0.3$. The optical counterpart to the central bright radio source shown in the high resolution contours (denoted by the green box) has a spectroscopic redshift of $z = 0.76991$ (Ahumada et al. 2020). Another nearby source, which looks to be in the same cluster, also has a spectroscopic redshift of $z = 0.76391$. For these reasons, we adopt a redshift of $z = 0.76991$ for this cluster.

Correcting the X-ray luminosity given by the MCXC for this change in redshift, we find a mass estimate of $M_{500} = 3.3^{+1.1}_{-1.7} \times 10^{14} M_\odot$. using the relation between L_{500} and M_{500} found by Arnaud et al. (2010). The one sigma error reported is underestimated, as this only takes into account the intrinsic scatter in the $L_X - M$ relation.

While masses derived from X-ray luminosity are generally less well constrained than masses derived from the Sunyaev-Zel'dovich effect, the fact that the cluster is not present in the *Planck* Sunyaev Zel'dovich catalogue (Planck Collaboration XXVII 2016) can also be used to constrain the mass. From visual inspection of the Compton parameter maps released by Planck Collaboration XXII (2016), we note that there are various detections in a region of four degrees around this cluster, which makes it likely that the non-detection of this cluster is simply due to a low signal-to-noise ratio and thus low mass of the cluster. The completeness of the PSZ2 catalogue as a function of mass and redshift (Fig. 26 in Planck Collaboration XXVII 2016) indicates that for the cluster redshift of $z = 0.76991$, the catalogue is 50% and 80% complete for masses of ~6.0 and ~7.5 $\times 10^{14} M_\odot$ respectively. This provides us a fiducial upper limit to the mass of the cluster of $\sim 7.5 \times 10^{14} M_\odot$).

The compact source subtraction process for this cluster is shown in Fig. 1. The final panel shows a clear detection of

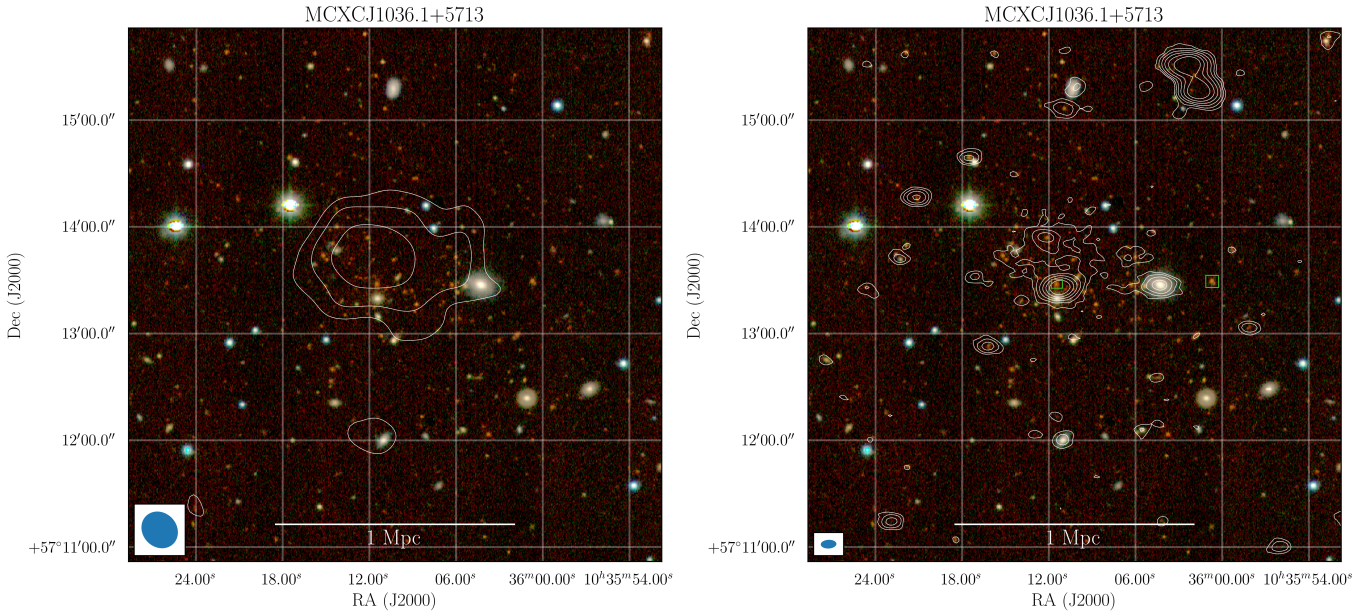

Fig. 6. Optical image (*grz* filters) of the cluster MCXCJ1036.1+5713 from the Legacy Survey with compact source subtracted low-resolution ($22'' \times 19''$) LOFAR contours overlaid (*left*) and high resolution compact source contours overlaid (*right*). Contours at $[3, 6, 12]\sigma$, where $\sigma = 86$ and 38 μJy beam^{-1} respectively. The green boxes denote the galaxies with SDSS spectra available.

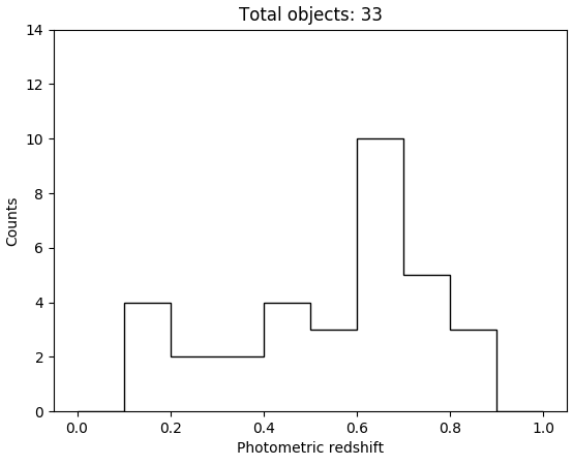

Fig. 7. SDSS photometric redshifts of galaxies within a radius of roughly $1.5r$ from the central radio source of the cluster MCXCJ1036.1+5713.

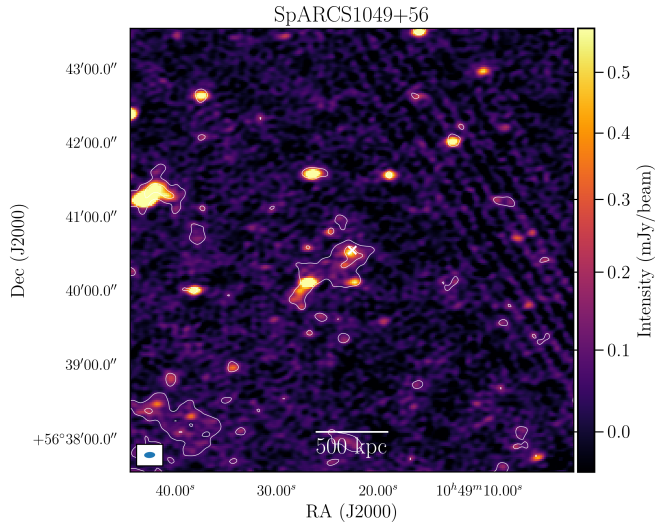

Fig. 8. High-resolution ($9'' \times 5''$) LOFAR radio intensity image of SpARCS1049+56 with low-resolution ($14'' \times 9''$) compact source subtracted contours showing diffuse emission at $[3, 6]\sigma$, where $\sigma = 48 \mu$Jy beam^{-1}. The white cross marks the location of the brightest cluster galaxy.

extended diffuse radio emission, which can be best observed from the radio-optical overlay given in Fig. 6. Because of the large size of this emission (>800 kpc), we classify this source as a radio halo.

We find best-fit parameters $I_0 = 7.7 \pm 0.5\,\mu$Jy arcsec^{-2} and $r_e = 124 \pm 7$ kpc. Integrating the analytical profile given in Eq. (1) results in a flux density of 9.8 ± 1.1 mJy. Assuming a spectral index of -1.5 ± 0.2, this translates to a radio luminosity of $P_{1.4\mathrm{GHz}} = (1.2 \pm 0.4) \times 10^{24}$ W Hz^{-1} at 1.4 GHz[3].

5.5. SpARCS1049+56

SpARCS1049+56 is a very high redshift ($z = 1.71$) cluster where star formation is actively taking place in the core, at a rate of 860 ± 130 $M_\odot$ yr^{-1} (Webb et al. 2015). The mass of the cluster was determined via infrared weak lensing to be $M_{200} = (3.5 \pm 1.2) \times 10^{14}$ $M_\odot$ (Finner et al. 2020).

We pick up some diffuse emission from this cluster. The compact source subtracted radio contours overlaid on the high-resolution radio map are shown in Fig. 8. The radio-optical overlay is shown in Fig. B.4. As the cluster is located at such a high redshift, it is difficult to properly subtract the compact sources from the diffuse component. It is clear that there is still some AGN-related emission contributing to the low-resolution contours, given the correlation between compact source locations and the location of the diffuse emission.

[3] For completeness we note that assuming a redshift of $z = 0.203$ would give a mass of $M_{500} = 0.88 \times 10^{14} M_\odot$ and a radio luminosity of $P_{1.4\mathrm{GHz}} = (3.8 \pm 1.7) \times 10^{24}$ W Hz^{-1}.

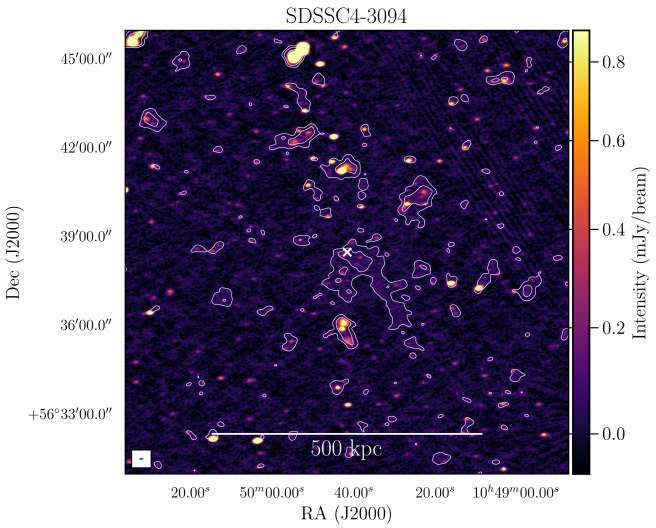

Fig. 9. SDSSC4-3094 LOFAR radio intensity map with a restoring beam of $9'' \times 5''$, with low-resolution ($21'' \times 19''$) compact source subtracted contours showing diffuse emission at $[3, 6, 12..]\sigma$, where $\sigma = 74\,\mu$Jy beam^{-1}. The white cross marks the location of the brightest cluster galaxy.

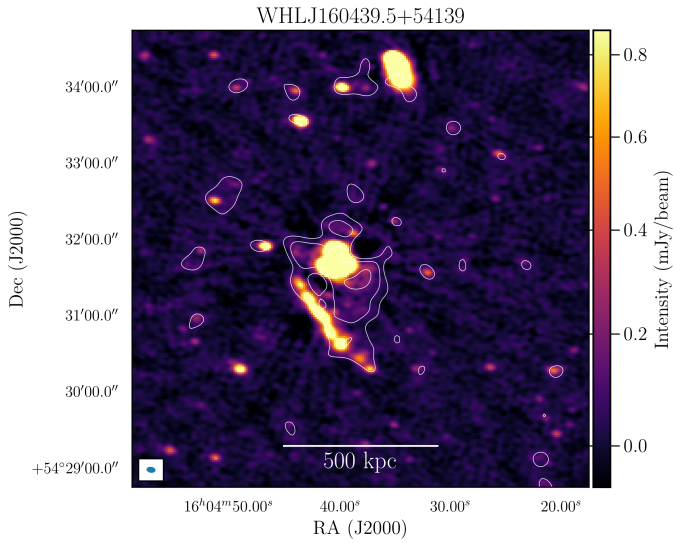

Fig. 10. WHLJ160439.5+543139 high-resolution ($7'' \times 5''$) LOFAR radio intensity image with low-resolution ($17'' \times 15''$) compact source subtracted contours at $[3, 6, 12, ..]\sigma$, where $\sigma = 72\,\mu$Jy beam^{-1}.

We believe that the emission that is being picked up in the core is most likely AGN related, also because radio halos are expected to be intrinsically less luminous (by a factor of $B^2/B^2_{\rm CMB}$) with higher redshift due to inverse Compton losses (e.g. Enßlin & Röttgering 2002; Cassano et al. 2006, 2019). Even assuming a magnetic field of a few μG for the cluster at $z = 1.71$ (e.g. Domínguez-Fernández et al. 2019), the synchrotron radiation would be reduced by about two orders of magnitude, making the detection of such a halo extremely unlikely by simple energetic arguments.

5.6. SDSSC4-3094

A nearby galaxy cluster, SDSSC4-3094, identified in the Sloan Digital Sky Survey (Miller et al. 2005) at $z = 0.04632 \pm 0.00083$ happens to be located in the same extracted region as SpARCS1049+56. The radio-optical overlay is shown in Appendix B (Fig. B.5). From this cluster we detect diffuse emission shown in Fig. 9 to the south-west of the BCG. This emission is not following the radio galaxy distribution and seems like genuine diffuse emission. However, it is likely not a radio halo, given the one-sided morphology. to the south-east. We classify this emission as remnant AGN emission due to this morphology and low surface brightness.

5.7. Upper limits on non-detections

The three WHL clusters that we identified showing possible diffuse emission are fairly unknown clusters. All radio-optical overlays for the WHL clusters are shown in Appendix B. Because these are optically detected clusters, we can estimate their mass from the richness. We use the relation given by Wen et al. (2012)

$$\log M_{200} = (-1.49 \pm 0.05) + (1.17 \pm 0.03) \log R_{L^*} \quad (5)$$

where R_{L^*} is the cluster richness as reported in Wen et al. (2012) and M_{200} is the mass in units of $10^{14} M_\odot$. To convert the masses to M_{500} we use $M_{500} = 0.72\ M_{200}$, which assumes a Navarro-Frenk-White profile with a concentration parameter $c = 5$ for the cluster scale dark matter halo (Navarro et al. 1996; Pierpaoli et al. 2003).

The results of the subtract and extract procedure are briefly stated per cluster.

WHLJ160439.5+543139. This cluster is located at a redshift of $z = 0.2655$ and shows a head-tail radio galaxy to the south-east of the likely BCG (Fig. 10). From the richness we estimate a mass $M_{500} = (2.95 \pm 0.50) \times 10^{14} M_\odot$. We tentatively detect diffuse emission surrounding the BCG, but due to the complexity of the emission from a head-tail radio galaxy, the AGN emission cannot be fully subtracted. To provide an upper limit on a halo detection, we inject halos slightly east of the cluster, in a region without contaminating radio sources. Following the correlations mentioned in Sect. 3.2, we initially set $I_0 = 7.7\mu$Jy arcsec^{-2} and $r_e = 65$ kpc. We find that the halo is easily detected for these values, as shown in the first panel of Fig. 11. The resulting upper limit is found for $I_0 = 2.4\mu$ Jy arcsec^{-2}, as is shown in the bottom left panel of Fig. 11. This results in an integrated flux density of 3.0 mJy, which translates to an upper limit on the radio power at 144 MHz of $P_{144\rm MHz} = 7.4 \times 10^{23}$ W Hz^{-1}.

WHLJ161135.9+541635. This cluster lies at a redshift of $z = 0.3407$, with an estimated mass of $M_{500} = (3.4 \pm 0.6) \times 10^{14} M_\odot$ and was selected visually because there seemed to be diffuse emission around the likely BCG in the wide-field image. However, after extraction and subtraction, no diffuse emission was detected, as shown in Fig. 12. For this cluster we find an upper limit for the values $I_0 = 3.5\mu$Jy arcsec^{-2}and $r_e = 80$ kpc, corresponding to a total flux density of 4.4 mJy. This translates to an upper limit of $P_{144\rm MHz} = 2.0 \times 10^{24}$ W Hz^{-1}.

WHLJ161420.1+544254. This WHL cluster also has a rather complex radio morphology, which combined with the leftover calibration artefacts prohibited the clear separation of AGN and diffuse emission (Fig. 13). The cluster lies at a redshift of $z = 0.3273$ with a mass of $M_{500} = (2.85 \pm 0.50) \times 10^{14} M_\odot$. For this cluster we find an upper limit for the values $I_0 = 3.1\mu$Jy arcsec^{-2} and $r_e = 64$ kpc, corresponding to an integrated flux density of 2.6 mJy and a radio power of $P_{144\rm MHz} = 1.1 \times 10^{24}$ W Hz^{-1}.

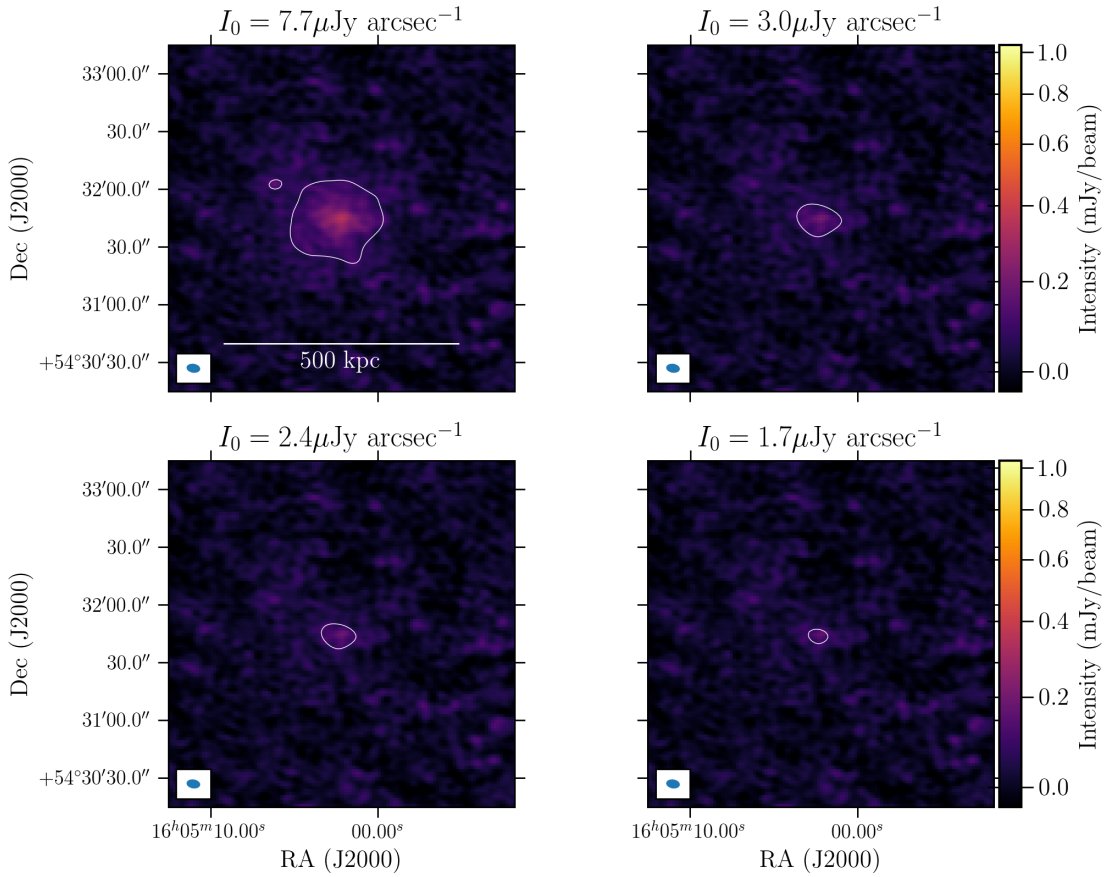

Fig. 11. Injected mock halos with decreasing surface brightness near the cluster WHLJ160439.5+543139. Contours are plotted at 3σ, where $\sigma = 25\,\mu$Jy beam^{-1}. The halo is still defined as detected in the *bottom left panel*, but not defined as detected in the *bottom right panel*.

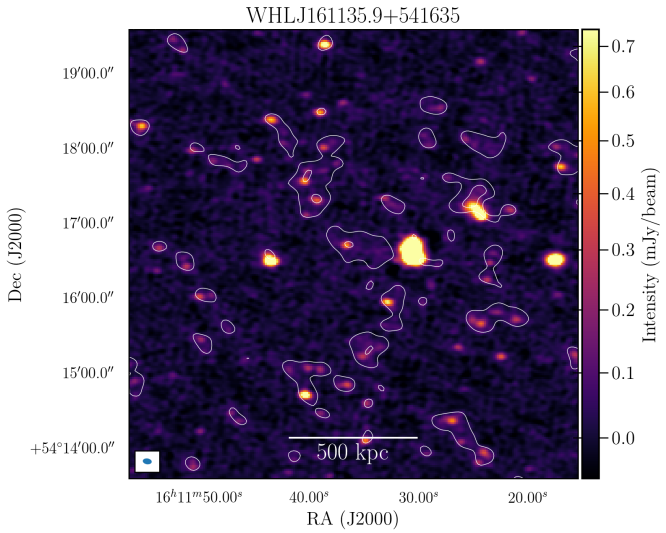

Fig. 12. WHLJ161135.9+541635 high-resolution ($7'' \times 5''$) LOFAR radio intensity image with low-resolution ($20'' \times 18''$) compact source subtracted contours at $[3, 6, 12, ..]\sigma$, where $\sigma = 62\,\mu$Jy beam^{-1}.

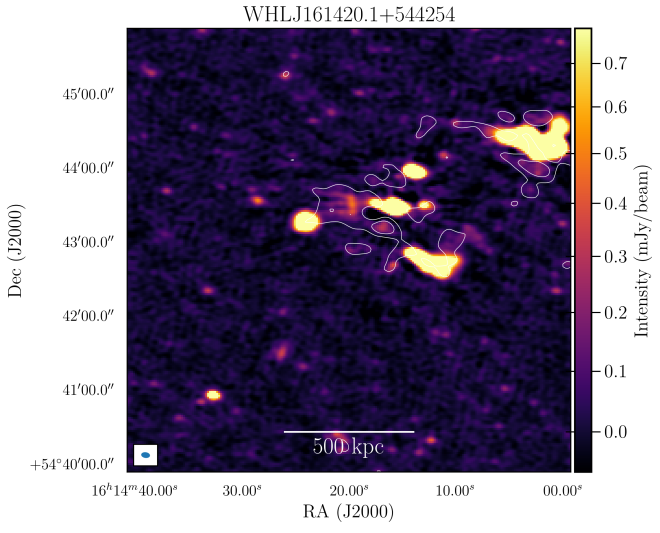

Fig. 13. WHLJ161420.1+544254 high-resolution ($7'' \times 5''$) LOFAR radio intensity image with low-resolution ($16'' \times 13''$) compact source subtracted contours at $[3, 6, 12, ..]\sigma$, where $\sigma = 66\,\mu$Jy beam^{-1}.

PSZRX G084.01+46.28. or Abell 2149 is quoted to have a redshift of 0.1068 in the PSZ2 and MCXC catalogues, however it has been identified as a duplicate cluster with a redshift measurement discrepancy of more than 10 per cent in the MCXC catalogue (see Table B.1. of Piffaretti et al. 2011). Rines & Diaferio (2006) also noted the discrepancy between the redshift of 0.1068 quoted by the NORAS catalogue (Böhringer et al. 2000) and $z = 0.0675$ in the eBCS catalogue (Ebeling et al. 2000). They noticed that the X-ray peak of the RASS image lies near an apparent BCG at the lower redshift. We adopt for this source the lower redshift of 0.0675 as well, since, as is shown in Fig. 14 the radio emission is also concentrated around

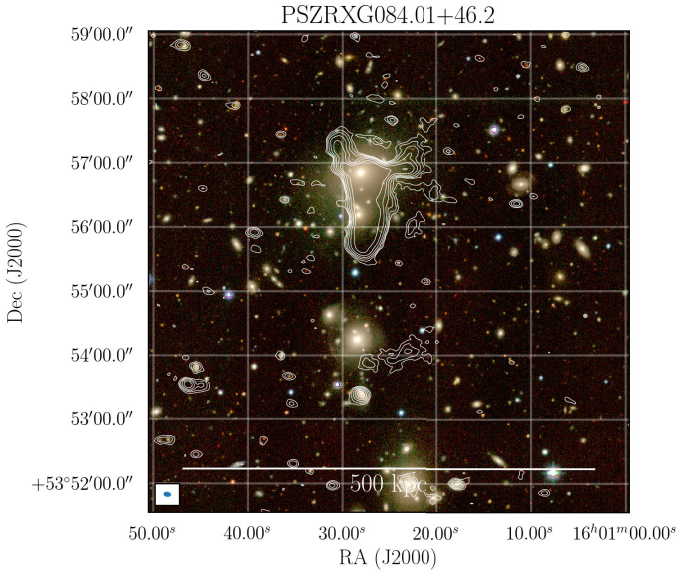

Fig. 14. Optical (*grz* filters) image from the Legacy survey with high-resolution ($7'' \times 5''$) LOFAR radio contours overlaid for the cluster PSZRXG084.01+46.28. Contours are spaced at $[3, 6, 12, ..]\sigma$ where $\sigma = 39\,\mu$Jy beam^{-1}.

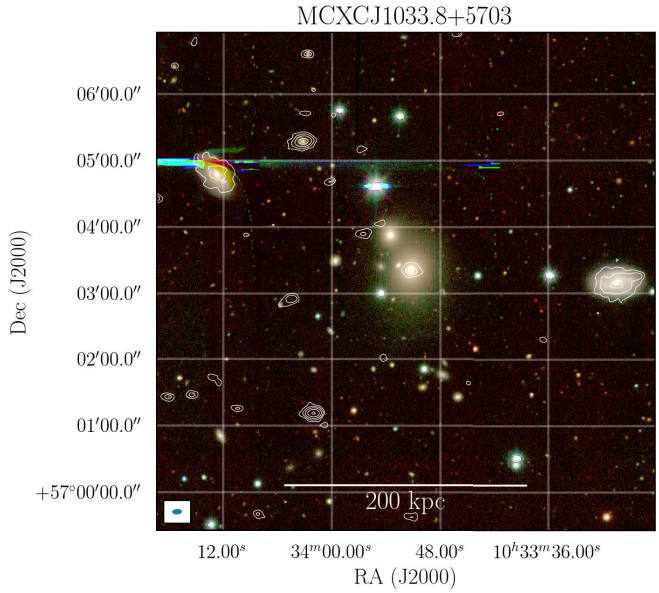

Fig. 15. Optical (*grz* filters) image from the Legacy survey with high-resolution ($9'' \times 5''$) LOFAR radio contours overlaid for the cluster MCXCJ1033.8+5703. Contours are spaced at $[3, 6, 12, ..]\sigma$ where $\sigma = 48\,\mu$Jy beam^{-1}.

the brightest cluster galaxy (BCG; at coordinates 16h01m28.10s +53°56m:50.8s) which is located at a redshift of $z = 0.06544$ (Ahn et al. 2013).

Since the redshift was overestimated, the mass of this cluster is overestimated as well. We calculate the corrected mass by assuming $z = 0.0675$ and interpolating the mass-redshift degeneracy curve given by the ComPRASS catalogue (Tarrío et al. 2019). This results in a corrected cluster mass of $M_{500} = 1.37^{+0.25}_{-0.27} \times 10^{14} M_{\odot}$.

This cluster is a difficult case since there is extended AGN emission surrounding the BCG, with a peculiar, bull head-like shape. Therefore, the central part of a radio halo would be obscured. However, the bull-head feature is quite narrow and we see no clear extended emission outside of it. We derive an upper limit by injection of a mock halo close to the cluster. The value of r_e found by following the correlations mentioned in Sect. 3.2 is only 25 kpc because of the low mass of this cluster. We choose to set $r_e = 65$ kpc, as diffuse sources with an r_e of 25 kpc would generally not be classified as a radio halo. Setting a larger e-folding radius results a more conservative upper limit. The upper limit for the peak surface brightness I_0 is found to be 2.5 μJy arcsec^{-2}, which results in a total flux density of 29 mJy or a radio power of $P_{144\mathrm{MHz}} = 3.3 \times 10^{23}$ W Hz^{-1}.

MCXC J1033.8+5703. No diffuse emission is picked up from this cluster (Fig. 15 shows the optical emission with overlaid radio contours), which is not unexpected given the low mass of $M_{500} = 0.128 \times 10^{14} M_{\odot}$ (Piffaretti et al. 2011). If the mass is correct, this particular source is closer to a galaxy group than a galaxy cluster. Some galaxy groups have detected extended synchrotron emission, but their origin is not fully clear (e.g. Giacintucci et al. 2011; Nikiel-Wroczyński et al. 2017, 2019). Because is it unknown whether such low mass configurations of galaxies can host radio halos, we do not provide an upper limit for this cluster.

MCXC J1053.3+5720. This cluster is quite a low mass cluster according to the MCXC derived mass of

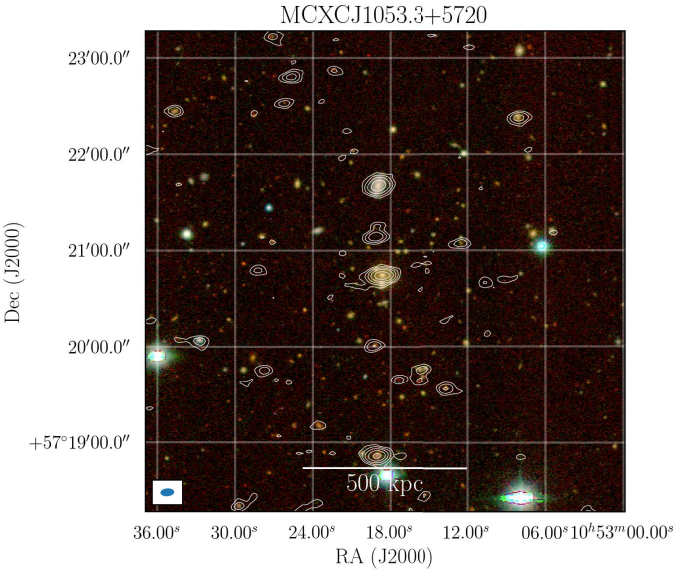

Fig. 16. Optical (*grz* filters) image from the Legacy survey with high-resolution ($9'' \times 5''$) LOFAR radio contours overlaid for the cluster MCXCJ1053.3+5720. Contours are spaced at $[3, 6, 12, ..]\sigma$ where $\sigma = 32\,\mu$Jy beam^{-1}.

$M_{500} = 0.487 \times 10^{14} M_{\odot}$ (Piffaretti et al. 2011). It shows no diffuse emission in Fig. 16, as is expected from such a low mass cluster. Although the mass is at least above a few times $10^{13} M_{\odot}$, the MCXC derived mass is still about a factor of five lower than the lowest mass cluster with a halo detection. Therefore, we do not consider it informative to provide an upper limit on such a cluster.

6. Discussion

To quantify the robustness of the fitting procedure used to estimate the flux density of the diffuse emission in this paper, we

Table 3. Resulting best-fit values for I_0 and r_e, as well as the total flux density $S_\nu^{\rm fit}$ from integrating the spherical model with the best-fit values.

Source name	$I_0[\mu$Jy arcsec$^{-2}]$	r_e[kpc]	$S_\nu^{\rm fit}$	d	$S_\nu^{\rm dfit}$	$S_\nu^{3\sigma}$	$S_\nu^{2.6r_e}$	$\chi^2_{\rm red}$
PSZ2G147.88+53.24	$4.4^{+0.3}_{-0.3}$	194^{+11}_{-10}	16.9 ± 2.0	2.5	16.4 ± 2.0	14.7 ± 1.6	16.0 ± 1.8	0.79
PSZ2G147.88+53.24 (mask)	$4.5^{+0.3}_{-0.3}$	186^{+11}_{-11}	16.0 ± 2.0	2.2	14.0 ± 1.7	13.0 ± 1.4	15.5 ± 1.7	0.79
PSZ2G149.22+54.18	$5.7^{+0.1}_{-0.1}$	235^{+4}_{-3}	244.9 ± 29.7	2.5	236.8 ± 29.0	261.0 ± 30.6	271.3 ± 31.7	1.24
PSZ2G084.69+42.28	$2.0^{+0.7}_{-0.6}$	57^{+18}_{-13}	5.5 ± 1.6	1.9	4.3 ± 1.2	3.4 ± 0.5	4.7 ± 0.8	0.05
MCXCJ1036.1+5713	$7.7^{+0.5}_{-0.5}$	124^{+7}_{-6}	9.8 ± 1.1	3.6	11.7 ± 1.3	9.9 ± 1.1	8.6 ± 0.9	0.57

Notes. Parameter d denotes half of the largest linear size of the 3σ contours in e-folding radii, and $S_\nu^{\rm dfit}$ is the flux density obtained by integrating up to that value of d. $S_\nu^{3\sigma}$ is the flux density measured within 3σ (2σ for PSZ2G084.69+42.28) contours and $S_\nu^{2.6r_e}$ is the flux density measured in a spherical region with a radius of $2.6r_e$.

compare the fitted flux densities to flux densities measured in various other ways. Table 3 shows the best-fit values of I_0 and r_e, as well as a comparison with the flux density measured within 3σ contours ($S_\nu^{3\sigma}$) and the flux density measured in a spherical region with a radius of $2.6r_e$ ($S_\nu^{2.6r_e}$). We find generally good agreement of the flux density measured within 3σ contours and the flux density from integrating the best-fit model, indicating that setting $d = 2.6$ and using a circular model are reasonable choices for the clusters presented here. The only outlier is the source MCXCJ1036.1+5713, where the 3σ contours extend beyond $2.6e$-folding radii, and the actual flux density of the diffuse emission is thus slightly larger than the value of 9.8 ± 1.1 that is found by integration of the best-fit model. Integrating the model up to the value of $d = 3.6$ results in a flux density of 11.7 ± 1.3 mJy.

We have found diffuse emission from three galaxy clusters in this study. One cluster hosts a new high-redshift radio halo, PSZ2G084.69+42.28, and two have been observed previously with shallower LOFAR observations, PSZ2 G147.88+53.24 and PSZ2 G149.22+54.18. We tentatively detect diffuse emission from the cluster PSZ2G084.69+42.28, but this has to be confirmed with upcoming deeper data releases. Upper limits have been put on the clusters PSZRX G084.01+46.28, WHL J160439.5+543139, WHL J161135.9+541635 and WHL J161420.1+544254. These results are compared to the well-known scaling relation between radio halo power and cluster mass from Cassano et al. (2013) derived for massive ($M_{500} > 5 \times 10^{14}$) clusters. This is shown in Fig. 17. We find that the radio power of the diffuse emission in the low mass clusters PSZ2G084.69+42.28 and MCXCJ1036.1+5713 are inconsistent with the statistical error on the best fit radio halo power - cluster mass correlation observed for higher mass systems. However, given the fact that radio halos are expected to scatter intrinsically around the correlation due to the different intrinsic properties of galaxy clusters and the different properties of mergers (Brunetti et al. 2009), two data points are not yet enough to conclude a significant deviation.

The turbulent re-acceleration model states that radio halos are caused by merger-induced turbulence in the intra-cluster medium (ICM) which re-accelerates relativistic electrons. A key prediction of this model is that lower mass clusters have less energetic merger events and thus less turbulent energy is being transferred to accelerate particles, leading to less powerful and steeper spectra radio halos (Brunetti & Jones 2014). These halos can only be picked up by sensitive low-frequency instruments. Calculations based on the turbulent re-acceleration model predict 1000–3000 halos with an integrated flux density at 150 MHz of 10 mJy in the whole sky (Cassano et al. 2006; Li et al. 2019).

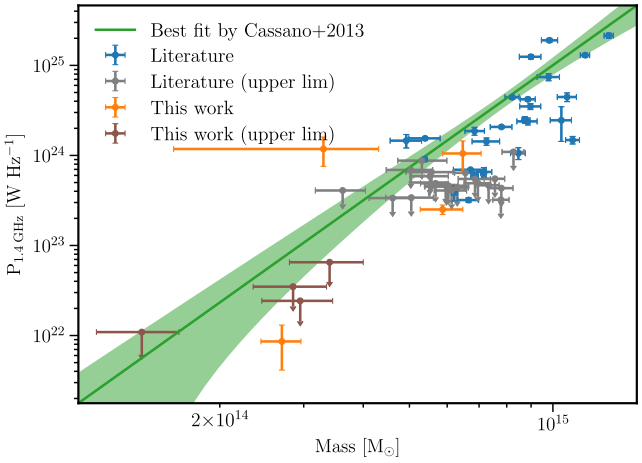

Fig. 17. Radio halo power–mass diagram for the clusters in this work and a sample of clusters from van Weeren et al. (2019) (Fig. 9) and references therein. The best-fit relation for radio halos, with the shaded 95% confidence region, from Cassano et al. (2013) is shown in green. We note that individual halos can easily scatter outside of the shaded region due to the intrinsic scatter of host cluster properties. For the sources in this work where the spectral index is unknown, we have assumed $\alpha = -1.5 \pm 0.2$.

The three fields considered in this work cover an area of about 60 deg^2, thus we would expect about 3 radio halo detections above an integrated flux density of 10 mJy. The results presented in this work are in line with these predictions.

Our study shows the potential of deep LOFAR observations to detect diffuse emission from galaxy clusters with masses below $5 \times 10^{14} M_\odot$, thus entering a poorly explored territory. In the 8 h LOFAR observations from the LOFAR Two Metre Sky Survey (Shimwell et al. 2019), the diffuse emission in PSZ2G084.69+42.28 is undetected and the diffuse emission in MCXCJ1036.1+5713 is barely detectable. Diffuse emission in a few other low mass clusters have been detected previously with LOFAR (e.g. Shimwell et al. 2016; Hoang et al. 2019; Botteon et al. 2019; Mandal et al. 2020). The diffuse emission found in PSZ2G084.69+42.28 and MCXCJ1036.1+5713 are important additions to the sparse sample of low mass ($<5 \times 10^{14} M_\odot$) clusters.

Theoretically, due to the lower turbulent energy budget in these low mass systems, the secondary electrons from hadronic collisions may become the dominant source for powering radio halos (e.g. Cassano et al. 2012). The transition from re-acceleration to hadronic halos depends on several unknowns,

such as the energy budget of cosmic-ray protons (CRp) in clusters and the extension of the regions where turbulent energy is dissipated into re-acceleration of particles. Models that assume that the energy budget of CRp is at the levels constrained by *Fermi*-LAT upper limits and that turbulence is dissipated in Mpc^3 regions (independent of cluster mass) predict a transition to hadronic halos at typical 150 MHz luminosities of $\sim 10^{24}\,\mathrm{W\,Hz^{-1}}$ (e.g. Cassano et al. 2012). This value is similar to the radio luminosity found in PSZ2G084.69+42.28 and the upper limits obtained in this study, showing that deep observations with LOFAR can potentially constrain this transition.

To investigate the possibility of a transition observationally, it is important to determine the dynamical state of the studied clusters. If radio halos in low mass clusters are still strongly connected to merger events, then that would suggest that the re-acceleration model still plays the dominant role, with implications on the extension of the turbulent regions and on the energy budget of CRp. The dynamical state of PSZ2G084.69+42.28 is also important to properly classify the diffuse emission.

Higher frequency follow-up observations are useful to differentiate between the two particle acceleration mechanisms. We have checked the ancillary 610 MHz GMRT observations of the ELAIS-N1 and Lockman Hole fields taken by Garn et al. (2008a,b), but unfortunately all PSZ2 and MCXC sources are just outside of the field-of-view of the GMRT observations. The WHL sources are observed, but show no sign of diffuse emission in the GMRT images. If, in future studies the spectral index of radio halos in low-mass sources is found to be very steep $\alpha \lessapprox -1.5$ a significant hadronic contribution will be ruled out (e.g. Pfrommer & Enßlin 2004; Brunetti et al. 2008).

The discovery of a radio halo in MCXCJ1036.1+5713 is particularly intriguing due to the combination of relatively low mass ($M_{500} \sim 3.3 \times 10^{14}$) and high redshift ($z = 0.76991$). Models predict a gradual decline of the fraction of clusters with radio halos at high redshift (e.g. Cassano et al. 2006). The observed decline is less prominent at low frequencies due to the increasing population of very steep spectrum halos that are expected to be more common at high redshift. Depending on the clusters magnetic field strength, a fraction of halos up to 10–25% in clusters with $M_{500} \sim (3\text{–}4) \times 10^{14} M_{\odot}$ at a redshift of 0.7 is predicted to be observed with LOFAR (Cassano et al. 2019). Better X-ray data with modern telescopes are needed to obtain a good estimate of the cluster mass and dynamical state.

Finally, our deeper images confirm that PSZ2G149.22+54.18 (Abell 1132) is hosting an under-luminous and steep-spectrum radio halo, which supports the idea that Abell 1132 is in a late merger state with weak turbulence (Wilber et al. 2017). Due to the high sensitivity of the current data, we see the halo emission blending with the outer edge of the giant head-tail radio galaxy. The possibility has been raised that gently re-energised tails (GreETs; de Gasperin et al. 2017) can provide a seed population of relativistic electrons for the generation of the cluster-scale emission. The interplay between the giant head-tail radio galaxy and radio halo seems to corroborate this scenario, although observations at different frequencies are needed to properly map the spectral index over the western edge of the tail to identify whether gentle re-energisation is indeed powering the diffuse emission from the tail. This connection between head-tail radio galaxies and halo emission has been observed in a few other clusters as well (e.g. Rajpurohit et al. 2018; Mandal et al. 2019). We also identify a sharp front in the halo, annotated in Fig. 4. This could be indicating a shock or shear motions in the ICM, although it is not visible in the X-ray image presented in Wilber et al. (2017). It might also be a magnetic filament or a region of higher turbulence seen in projection. Filamentary emission has been identified in halos before (e.g. in Abell 2255; Govoni et al. 2005; Botteon et al. 2020a). To investigate the possible polarisation of the filament, deep higher frequency observations are required.

7. Conclusion

This study presented a search for diffuse emission in the deepest LOFAR 144 MHz observations ever taken. All *Planck* Sunyaev-Zel'dovich detected clusters (PSZ2; ComPRASS; Planck Collaboration XXVII 2016; Tarrío et al. 2019) and clusters from the Meta Catalogue of X-ray detected Clusters (MCXC; Piffaretti et al. 2011) that overlap with the Deep Fields were inspected. The halos were systematically fitted with spherically symmetrical exponential profiles using Markov chain Monte Carlo sampling to sample the likelihood function.

We have found a new radio halo in the low mass, high-redshift cluster MCXCJ1036.1+5713 ($z = 0.77$) and tentatively detect diffuse emission from the low mass cluster PSZ2G084.69+42.28 ($z = 0.13$). We have set deep upper limits on diffuse emission from clusters with a non-detection and for two clusters previously observed with LOFAR, PSZ2G147.88+53.24 and PSZ2G149.22+54.18, we confirm results in the literature.

This study has detected diffuse emission in a largely unexplored region of parameter space for galaxy clusters. The results were compared to the radio luminosity - cluster mass relation for radio halos found in the literature, and we found that this small sample of clusters is consistent with the correlation extrapolated to lower masses.

The results presented here underline the importance of deep low-frequency observations of galaxy clusters. As the LOFAR Deep Fields reach their final depths of 10–15 $\mu\mathrm{Jy\,beam^{-1}}$, we expect more low-mass clusters to show radio halos and to put more stringent upper limits on the radio luminosity of lower mass clusters, which will begin to allow a statistical study of a sample of radio halos in low mass clusters.

In the future, international baseline data will additionally be imaged, resulting in sub-arcsecond resolution images at the same depth. This will allow for better separation of AGN and diffuse emission, especially for mini-halos and high-redshift clusters.

Acknowledgements. We thank W. Williams for her plotting functions. E.O., R.Jv.W. and A.B. acknowledge support from the VIDI research programme with project number 639.042.729, which is financed by the Netherlands Organisation for Scientific Research (NWO). G.B., R.C., F.G., M.R. acknowledge support from INAF through mainstream program 'galaxy clusters science with LOFAR' 1.05.01.86.05. Ann.B. acknowledges support from the ERC-Stg DRANOEL n. 714245 and from the MIUR FARE grant "SMS". P.N.B. is grateful for support from the UK STFC via grant ST/R000972/1. M.Bo. acknowledges support from INAF under PRIN SKA/CTA FORECaST and from the Ministero degli Affari Esteri della Cooperazione Internazionale - Direzione Generale per la Promozione del Sistema Paese Progetto di Grande Rilevanza ZA18GR02. G.D.G. acknowledges support from the ERC Starting Grant ClusterWeb 804208. M.J.H. acknowledges support from the UK Science and Technology Facilities Council (ST/R000905/1). H.R. acknowledges support from the ERC Advanced Investigator programme NewClusters 321271. J.S. is grateful for support from the UK STFC via grant ST/R000972/1. LOFAR (van Haarlem et al. 2013) is the Low Frequency Array designed and constructed by ASTRON. It has observing, data processing, and data storage facilities in several countries, which are owned by various parties (each with their own funding sources), and that are collectively operated by the ILT foundation under a joint scientific policy. The ILT resources have benefited from the following recent major funding sources: CNRS-INSU, Observatoire de Paris and Université d'Orléans, France; BMBF, MIWF-NRW, MPG, Germany; Science Foundation Ireland (SFI), Department of Business, Enterprise and Innovation (DBEI), Ireland; NWO, The Netherlands; The Science and Technology Facilities Council, UK; Ministry of Science and

Higher Education, Poland; The Istituto Nazionale di Astrofisica (INAF), Italy. This research made use of the Dutch national e-infrastructure with support of the SURF Cooperative (e-infra 180169) and the LOFAR e-infra group. The Jülich LOFAR Long Term Archive and the German LOFAR network are both coordinated and operated by the Jülich Supercomputing Centre (JSC), and computing resources on the supercomputer JUWELS at JSC were provided by the Gauss Centre for Supercomputing e.V. (grant CHTB00) through the John von Neumann Institute for Computing (NIC). This research made use of the University of Hertfordshire high-performance computing facility and the LOFAR-UK computing facility located at the University of Hertfordshire and supported by STFC [ST/P000096/1], and of the Italian LOFAR IT computing infrastructure supported and operated by INAF, and by the Physics Department of Turin university (under an agreement with Consorzio Interuniversitario per la Fisica Spaziale) at the C3S Supercomputing Centre, Italy. This research has made use of NASA's Astrophysics Data System.

References

Ahn et al. 2013, VizieR Online Data Catalog: V/139
Ahumada, R., Prieto, C. A., Almeida, A., et al. 2020, ApJS, 249, 3
Arnaud, M., Pratt, G. W., Piffaretti, R., et al. 2010, A&A, 517, A92
Bîrzan, L., Rafferty, D. A., Cassano, R., et al. 2019, MNRAS, 487, 4775
Blasi, P., & Colafrancesco, S. 1999, Astropart. Phys., 12, 169
Böhringer, H., Voges, W., Huchra, J. P., et al. 2000, ApJS, 129, 435
Bonafede, A., Intema, H. T., Bruggen, M., et al. 2014, MNRAS, 444, L44
Bonafede, A., Cassano, R., Brüggen, M., et al. 2017, MNRAS, 470, 3465
Botteon, A., Cassano, R., Eckert, D., et al. 2019, A&A, 630, A77
Botteon, A., Brunetti, G., van Weeren, R. J., et al. 2020a, ApJ, 897, 93
Botteon, A., van Weeren, R. J., Brunetti, G., et al. 2020b, MNRAS, 499, L11
Boxelaar, J. M., van Weeren, R., & Botteon, A. 2021, Astron. Comput., submitted [arXiv:2103.08554]
Brüggen, M., Bykov, A., Ryu, D., & Röttgering, H. 2012, Space Sci. Rev., 166, 187
Brunetti, G., & Jones, T. W. 2014, Int. J. Mod. Phys. D, 23, 1430007
Brunetti, G., & Lazarian, A. 2007, MNRAS, 378, 245
Brunetti, G., & Lazarian, A. 2011, MNRAS, 410, 127
Brunetti, G., Venturi, T., Dallacasa, D., et al. 2007, ApJ, 670, L5
Brunetti, G., Giacintucci, S., Cassano, R., et al. 2008, Nature, 455, 944
Brunetti, G., Cassano, R., Dolag, K., & Setti, G. 2009, A&A, 507, 661
Brunetti, G., Blasi, P., Reimer, O., et al. 2012, MNRAS, 426, 956
Brunetti, G., Zimmer, S., & Zandanel, F. 2017, MNRAS, 472, 1506
Burenin, R. A., Vikhlinin, A., Hornstrup, A., et al. 2007, ApJS, 172, 561
Cassano, R. 2010, A&A, 517, A10
Cassano, R., Brunetti, G., & Setti, G. 2006, MNRAS, 369, 1577
Cassano, R., Brunetti, G., Setti, G., Govoni, F., & Dolag, K. 2007, MNRAS, 378, 1565
Cassano, R., Brunetti, G., Norris, R. P., et al. 2012, A&A, 548, A100
Cassano, R., Ettori, S., Brunetti, G., et al. 2013, ApJ, 777, 141
Cassano, R., Botteon, A., Di Gennaro, G., et al. 2019, ApJ, 881, L18
Cuciti, V., Cassano, R., Brunetti, G., et al. 2015, A&A, 580, A97
Dallacasa, D., Brunetti, G., Giacintucci, S., et al. 2009, ApJ, 699, 1288
de Gasperin, F., Intema, H. T., Shimwell, T. W., et al. 2017, Sci. Adv., 3, e1701634
Dey, A., Schlegel, D. J., Lang, D., et al. 2019, AJ, 157, 168
Di Gennaro, G., van Weeren, R. J., Brunetti, G., et al. 2021, Nat. Astron., 5, 268
Dolag, K., & Enßlin, T. A. 2000, A&A, 362, 151
Domínguez-Fernández, P., Vazza, F., Brüggen, M., & Brunetti, G. 2019, MNRAS, 486, 623
Donnert, J., Vazza, F., Brüggen, M., & ZuHone, J. 2018, Space Sci. Rev., 214, 122
Duncan, K. J., Kondapally, R., Brown, M. J. I., et al. 2021, A&A, 648, A4 (LoTSS SI)
Ebeling, H., Edge, A. C., Allen, S. W., et al. 2000, MNRAS, 318, 333
Eckert, D., Gaspari, M., Vazza, F., et al. 2017, ApJ, 843, L29
Eisenhardt, P. R. M., Brodwin, M., Gonzalez, A. H., et al. 2008, ApJ, 684, 905
Enßlin, T. A., & Röttgering, H. 2002, A&A, 396, 83
Feretti, L., Giovannini, G., Govoni, F., & Murgia, M. 2012, A&A Rev., 20, 54
Finner, K., James Jee, M., Webb, T., et al. 2020, ApJ, 893, 10
Foreman-Mackey, D., Hogg, D. W., Lang, D., & Goodman, J. 2013, Publ. ASP, 125, 306
Garn, T., Green, D. A., Riley, J. M., & Alexander, P. 2008a, MNRAS, 383, 75
Garn, T., Green, D. A., Riley, J. M., & Alexander, P. 2008b, MNRAS, 387, 1037
Giacintucci, S., O'Sullivan, E., Vrtilek, J., et al. 2011, ApJ, 732, 95
Giacintucci, S., Markevitch, M., Cassano, R., et al. 2017, ApJ, 841, 71
Giovannini, G., & Feretti, L. 2000, New Astron., 5, 335
Giovannini, G., Bonafede, A., Feretti, L., et al. 2009, A&A, 507, 1257
Giovannini, G., Feretti, L., Girardi, M., et al. 2011, A&A, 530, L5
Govoni, F., Murgia, M., Feretti, L., et al. 2005, A&A, 430, L5
Govoni, F., Murgia, M., Feretti, L., et al. 2006, A&A, 460, 425
Hardcastle, M. J., Croston, J. H., Shimwell, T. W., et al. 2019, MNRAS, 488, 3416
Hoang, D. N., Shimwell, T. W., van Weeren, R. J., et al. 2018, MNRAS, 478, 2218
Hoang, D. N., Shimwell, T. W., van Weeren, R. J., et al. 2019, A&A, 622, A21
Jannuzi, B. T., & Dey, A. 1999, ASP Conf. Ser., 191, 111
Jeltema, T. E., & Profumo, S. 2011, ApJ, 728, 53
Kale, R., Venturi, T., Giacintucci, S., et al. 2015, A&A, 579, A92
Kondapally, R., Best, P. N., Hardcastle, M. J., et al. 2021, A&A, 648, A3 (LoTSS SI)
La Franca, F., Fiore, F., Vignali, C., et al. 2002, ApJ, 570, 100
Li, W., Xu, H., Ma, Z., et al. 2019, ApJ, 879, 104
Liang, H., Hunstead, R. W., Birkinshaw, M., & Andreani, P. 2000, ApJ, 544, 686
Lockman, F. J., Jahoda, K., & McCammon, D. 1986, ApJ, 302, 432
Macario, G., Venturi, T., Intema, H. T., et al. 2013, A&A, 551, A141
Mandal, S., Intema, H. T., Shimwell, T. W., et al. 2019, A&A, 622, A22
Mandal, S., Intema, H. T., van Weeren, R. J., et al. 2020, A&A, 634, A4
Miller, C. J., Nichol, R. C., Reichart, D., et al. 2005, AJ, 130, 968
Miniati, F. 2015, ApJ, 800, 60
Murgia, M., Govoni, F., Markevitch, M., et al. 2009, A&A, 499, 679
Navarro, J. F., Frenk, C. S., & White, S. D. M. 1996, ApJ, 462, 563
Nikiel-Wroczyński, B., Urbanik, M., Soida, M., Beck, R., & Bomans, D. J. 2017, A&A, 603, A97
Nikiel-Wroczyński, B., Berger, A., Herrera Ruiz, N., et al. 2019, A&A, 622, A23
Offringa, A. R., & Smirnov, O. 2017, MNRAS, 471, 301
Offringa, A. R., McKinley, B., Hurley-Walker, N., et al. 2014, MNRAS, 444, 606
Oliver, S., Rowan-Robinson, M., Alexander, D. M., et al. 2000, MNRAS, 316, 749
Paul, S., Iapichino, L., Miniati, F., Bagchi, J., & Mannheim, K. 2011, ApJ, 726, 17
Pfrommer, C., & Enßlin, T. A. 2004, A&A, 413, 17
Pierpaoli, E., Borgani, S., Scott, D., & White, M. 2003, MNRAS, 342, 163
Piffaretti, R., Arnaud, M., Pratt, G. W., Pointecouteau, E., & Melin, J. B. 2011, A&A, 534, A109
Pinzke, A., Oh, S. P., & Pfrommer, C. 2017, MNRAS, 465, 4800
Planck Collaboration XXII. 2016, A&A, 594, A22
Planck Collaboration XXVII. 2016, A&A, 594, A27
Rajpurohit, K., Hoeft, M., van Weeren, R. J., et al. 2018, ApJ, 852, 65
Rines, K., & Diaferio, A. 2006, AJ, 132, 1275
Sabater, J., Best, P. N., Tasse, C., et al. 2021, A&A, 648, A2 (LoTSS SI)
Savini, F., Bonafede, A., Brüggen, M., et al. 2019, A&A, 622, A24
Shimwell, T. W., Luckin, J., Brüggen, M., et al. 2016, MNRAS, 459, 277
Shimwell, T. W., Röttgering, H. J. A., Best, P. N., et al. 2017, A&A, 598, A104
Shimwell, T. W., Tasse, C., Hardcastle, M. J., et al. 2019, A&A, 622, A1
Smirnov, O. M., & Tasse, C. 2015, MNRAS, 449, 2668
Sommer, M. W., Basu, K., Intema, H., et al. 2017, MNRAS, 466, 996
Struble, M. F., & Rood, H. J. 1991, ApJS, 77, 363
Tarrío, P., Melin, J. B., & Arnaud, M. 2019, A&A, 626, A7
Tasse, C. 2014, ArXiv e-prints [arXiv:1410.8706]
Tasse, C., Hugo, B., Mirmont, M., et al. 2018, A&A, 611, A87
Tasse, C., Shimwell, T., Hardcastle, M. J., et al. 2021, A&A, 648, A1 (LoTSS SI)
van Haarlem, M. P., Wise, M. W., Gunst, A. W., et al. 2013, A&A, 556, A2
van Weeren, R. J., Brunetti, G., Brüggen, M., et al. 2016, ApJ, 818, 204
van Weeren, R. J., de Gasperin, F., Akamatsu, H., et al. 2019, Space Sci. Rev., 215, 16
van Weeren, R. J., Shimwell, T. W., Botteon, A., et al. 2020, ArXiv e-prints [arXiv:2011.02387]
Venturi, T., Bardelli, S., Dallacasa, D., et al. 2003, A&A, 402, 913
Venturi, T., Giacintucci, S., Dallacasa, D., et al. 2008, A&A, 484, 327
Wang, Q. H. S., Giacintucci, S., & Markevitch, M. 2018, ApJ, 856, 162
Webb, T., Noble, A., DeGroot, A., et al. 2015, ApJ, 809, 173
Wen, Z. L., & Han, J. L. 2013, MNRAS, 436, 275
Wen, Z. L., Han, J. L., & Liu, F. S. 2012, ApJS, 199, 34
Wilber, A., Brüggen, M., Bonafede, A., et al. 2017, MNRAS, 473, 3536
Zandanel, F., & Ando, S. 2014, MNRAS, 440, 663

Appendix A: Surface brightness fits

We show in this appendix the azimuthally averaged surface brightness profiles, the best-fit model and the corner plots of the MCMC chain. To be clear, the fitting algorithm performs the fitting in the image plane, but because a spherically symmetrical model is assumed in this work the radial profiles contain all necessary information.

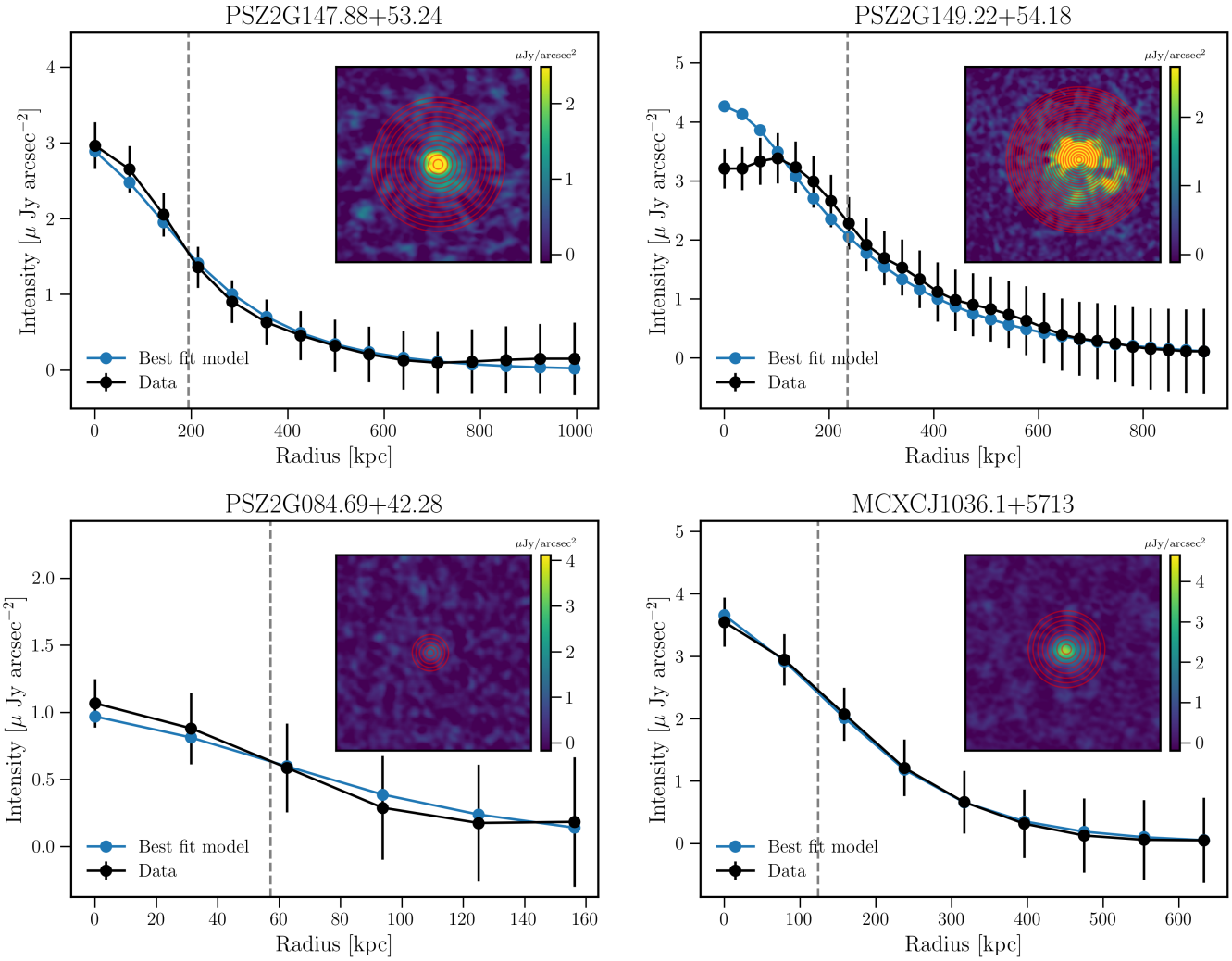

Fig. A.1. Azimuthally averaged surface brightness profiles for the clusters presented in this work. The inset images show the concentric annuli where the profile has been calculated, the width of the annuli is equal to the semi-major axis of the restoring beam. The dashed grey line indicates the best-fit *e*-folding radius.

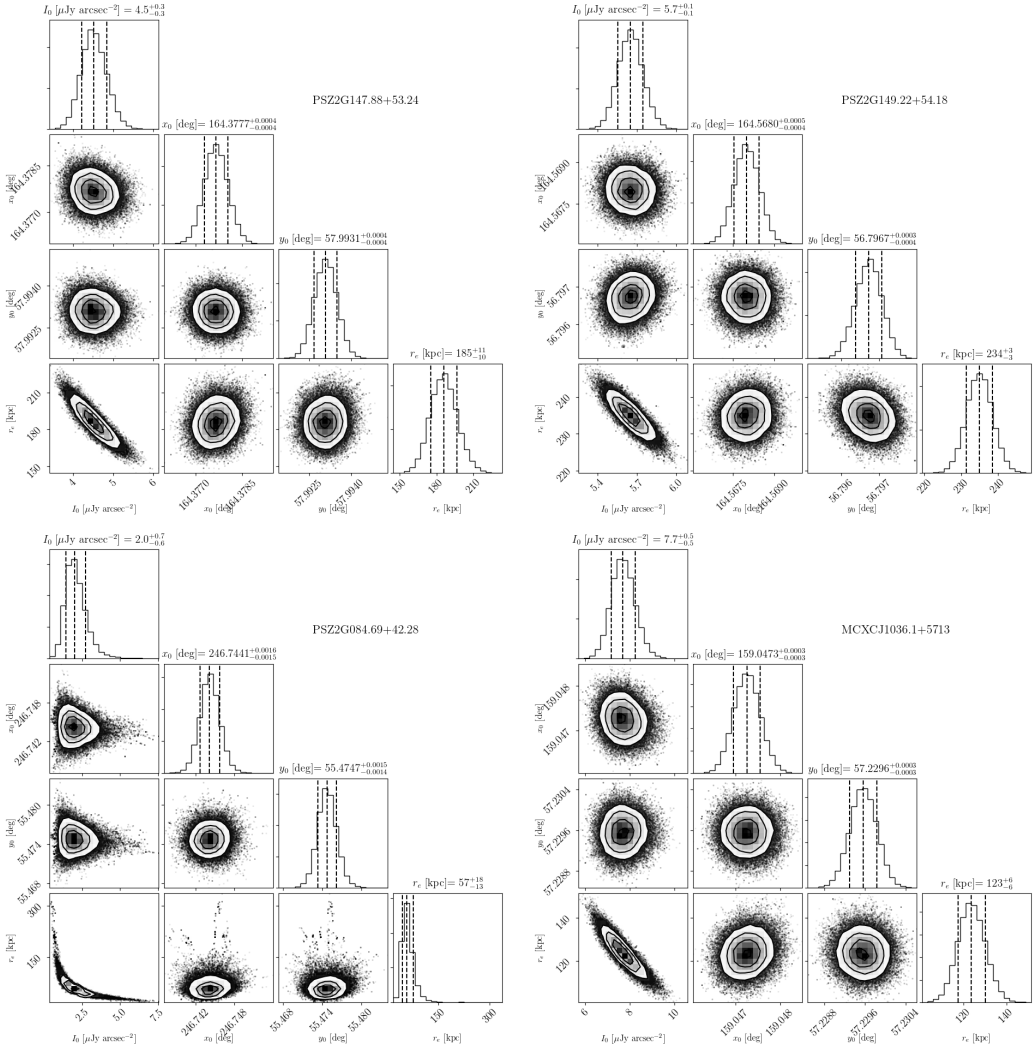

Fig. A.2. Corner plots of the fitted parameters given by the MCMC chain. The dashed lines indicate the 16, 50th and 84th percentiles of the chain.

Appendix B: Radio Optical overlays

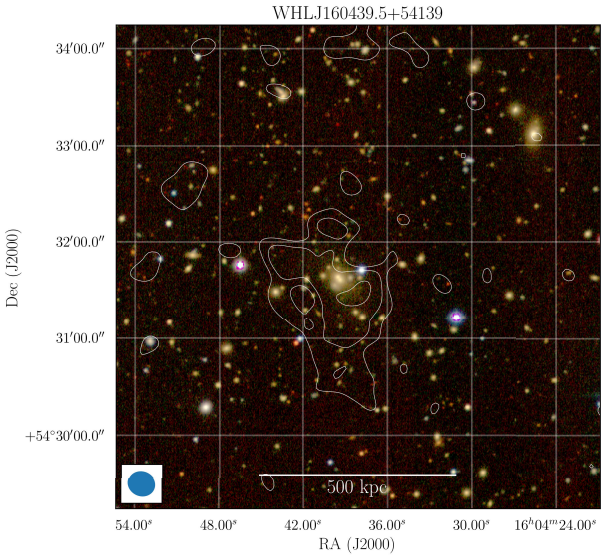

Fig. B.1. Optical (*grz*) image of WHLJ160439.5+54139 from the Legacy Survey with compact source subtracted low-resolution LOFAR contours overlaid. The beam size is $17'' \times 15''$. Contours at $[3, 6, 12, ..]\sigma$, where $\sigma = 72\,\mu$Jy beam^{-1}.

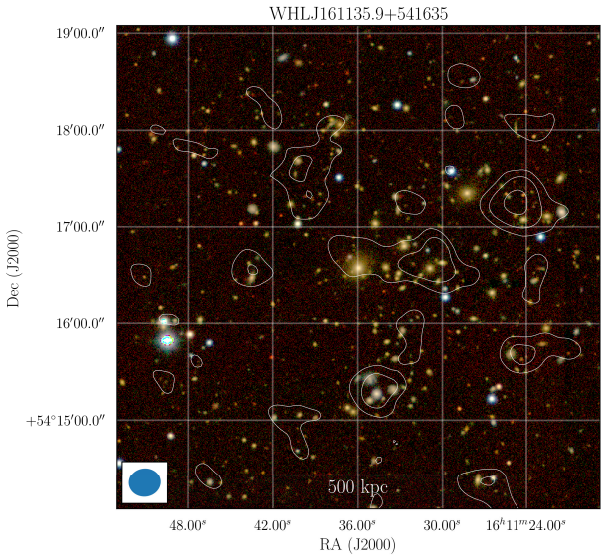

Fig. B.2. Optical (*grz*) image of WHLJ161135.9+541635 from the Legacy Survey with compact source subtracted low-resolution LOFAR contours overlaid. The beam size is $20'' \times 18''$. Contours at $[3, 6, 12, ..]\sigma$, where $\sigma = 62\,\mu$Jy beam^{-1}.

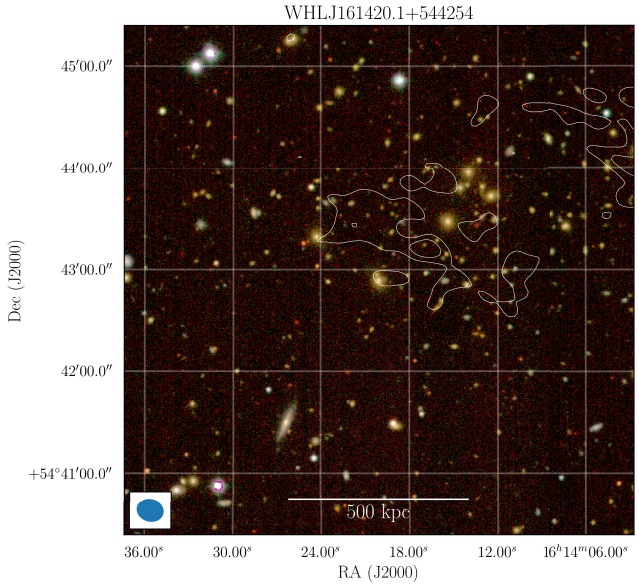

Fig. B.3. Optical (*grz*) image of WHLJ161420.1+544254 from the Legacy Survey with compact source subtracted low-resolution LOFAR contours overlaid. The beam size is $X16 \times 13''$. Contours at $[3, 6, 12, ..]\sigma$, where $\sigma = 66\,\mu$Jy beam^{-1}.

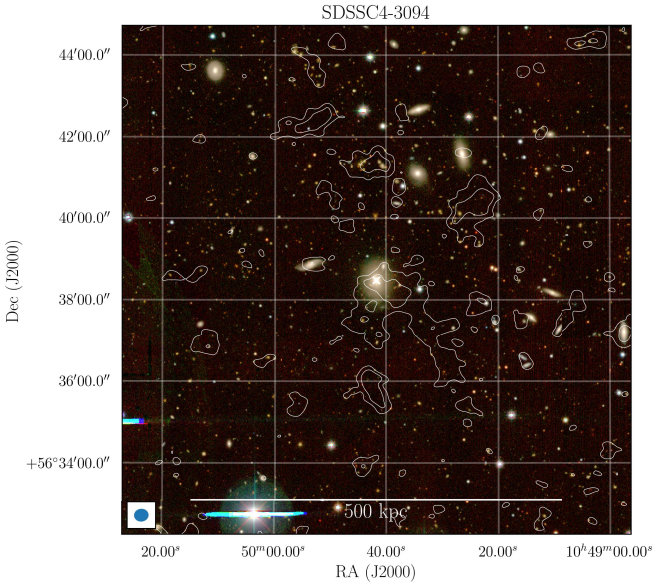

Fig. B.5. Optical (*grz*) image of SDSSC4-3094 from the Legacy Survey with compact source subtracted low-resolution LOFAR contours overlaid. The beam size is $21'' \times 19''$. Contours at $[3, 6, 12, ..]\sigma$, where $\sigma = 74\,\mu$Jy beam^{-1}.

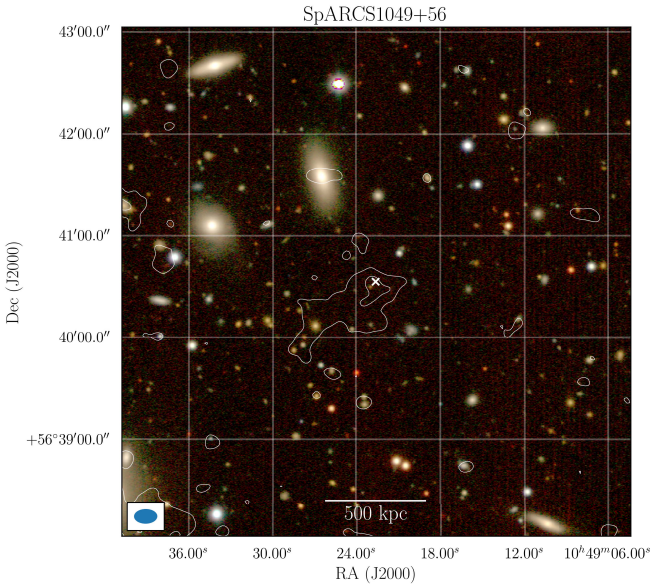

Fig. B.4. Optical (*grz*) image of SpARCS1049+56 from the Legacy Survey with compact source subtracted low-resolution LOFAR contours overlaid. The beam size is $14'' \times 9''$. Contours at $[3, 6]\sigma$, where $\sigma = 48\,\mu$Jy beam^{-1}.